

# Controls on Larsen C Ice Shelf retreat from a 60-year satellite data record

Shujie Wang<sup>1</sup>, Hongxing Liu<sup>2</sup>, Kenneth C. Jezek<sup>3</sup>, Richard B. Alley<sup>4</sup>, Lei Wang<sup>5</sup>, Patrick M. Alexander<sup>6</sup>, and Yan Huang<sup>7</sup>

<sup>1</sup>Penn State University

<sup>2</sup>University of Alabama

<sup>3</sup>Byrd Polar Research Center, The Ohio State University

<sup>4</sup>Pennsylvania State University

<sup>5</sup>Louisiana State University

<sup>6</sup>Lamont-Doherty Earth Observatory of Columbia University

<sup>7</sup>East China Normal University

November 21, 2022

## Abstract

Rapid retreat of the Larsen A and B ice shelves has provided important clues about the ice shelf destabilization processes. The Larsen C Ice Shelf, the largest remaining ice shelf on the Antarctic Peninsula, may also be vulnerable to future collapse in a warming climate. Here, we utilize multi-source satellite images collected over 1963–2020 to derive multidecadal time series of ice front, flow velocities, and critical rift features over Larsen C, with the aim of understanding the controls on its retreat. We complement these observations with modeling experiments using the Ice-sheet and Sea-level System Model to examine how front geometry conditions and mechanical weakening due to rifts affect ice shelf dynamics. Over the past six decades, Larsen C lost over 20% of its area, dominated by rift-induced tabular iceberg calving. The Bawden Ice Rise and Gipps Ice Rise are critical areas for rift formation, through their impact on the longitudinal deviatoric stress field. Mechanical weakening around Gipps Ice Rise is found to be a primary control on localized flow acceleration, leading to the propagation of two rifts that caused a major calving event in 2017. Capturing the time-varying effects of rifts on ice rigidity in ice shelf models is essential for making realistic predictions of ice shelf flow dynamics and instability. In the context of the Larsen A and Larsen B collapses, we infer a chronology of destabilization processes for embayment-confined ice shelves, which provides a useful framework for understanding the historical and future destabilization of Antarctic ice shelves.

Shujie Wang<sup>1,2,3</sup>, Hongxing Liu<sup>4,5</sup>, Kenneth Jezek<sup>6</sup>, Richard B. Alley<sup>2,7</sup>, Lei Wang<sup>8</sup>, Patrick Alexander<sup>9</sup>, and Yan Huang<sup>5</sup>

<sup>1</sup>Department of Geography, Pennsylvania State University, University Park, PA 16802, USA.

<sup>2</sup>Earth and Environmental Systems Institute, Pennsylvania State University, University Park, PA 16802, USA.

<sup>3</sup>Institute for Computational and Data Sciences, Pennsylvania State University, University Park, PA 16802, USA.

<sup>4</sup>Department of Geography, University of Alabama, Tuscaloosa, AL 35487, USA.

<sup>5</sup>Key Laboratory of Geographic Information Science, Ministry of Education, East China Normal University, Shanghai 200241, China.

<sup>6</sup>School of Earth Sciences, Ohio State University, Columbus, OH 43210, USA.

<sup>7</sup>Department of Geosciences, Pennsylvania State University, University Park, PA 16802, USA.

<sup>8</sup>Department of Geography & Anthropology, Louisiana State University, Baton Rouge, LA 70803, USA.

<sup>9</sup>Lamont-Doherty Earth Observatory, Columbia University, Palisades, NY 10964, USA.

Corresponding author: Shujie Wang (skw5660@psu.edu)

#### Key Points:

- Multidecadal satellite images and ice shelf modeling experiments were used to examine dynamic changes of Larsen C during 1963–2020
- Rift development near ice rises is a primary control on ice shelf retreat and flow acceleration before the compressive arch is reached
- Capturing the time-varying effects of rifts on ice rigidity is needed to make realistic simulations of future ice shelf change

#### Abstract

Rapid retreat of the Larsen A and B ice shelves has provided important clues about the ice shelf destabilization processes. The Larsen C Ice Shelf, the largest remaining ice shelf on the Antarctic Peninsula, may also be vulnerable to future collapse in a warming climate. Here, we utilize multi-source satellite images collected over 1963–2020 to derive multidecadal time series of ice front, flow velocities, and critical rift features over Larsen C, with the aim of understanding the controls on its retreat. We complement these observations with modeling experiments using the Ice-sheet and Sea-level System Model to examine how front geometry conditions and mechanical weakening due to rifts affect ice shelf dynamics. Over the past six decades, Larsen C lost over 20% of its area, dominated by rift-induced tabular iceberg calving. The Bawden Ice Rise and Gipps Ice Rise are critical areas for rift formation, through their impact on the longitudinal deviatoric stress field. Mechanical weakening around Gipps Ice Rise is found to be a primary control on localized flow acceleration, leading to the propagation of two rifts that caused a major calving event in 2017. Capturing the time-varying effects of rifts on ice rigidity in ice shelf models is essential for making realistic predictions of ice shelf flow dynamics and instability. In the context of the Larsen A and Larsen B collapses, we infer a chronology of destabilization processes for embayment-confined ice shelves, which provides a useful framework for understanding the historical and future destabilization of Antarctic ice shelves.

#### Plain Language Summary

The Antarctic Ice Sheet is the largest source of uncertainty in projecting future sea-level rise. This is due to our limited understanding of drivers and mechanisms triggering tipping points in ice-sheet instability, and knowledge gaps regarding the retreat and disintegration of ice shelves. Understanding processes leading to ice shelf destabilization is critical to improving estimates of future Antarctic mass loss because of their important role in stabilizing ice flow. We studied Larsen C Ice Shelf changes using satellite data collected over 1963–2020, and conducted modeling experiments to elucidate the observed linkages between front retreat, flow acceleration, and rifts. We find the development of rifts near ice rises to be the primary control on Larsen C front calving and flow acceleration in the past six decades. Rifts can affect each other by causing structural weakening and modifying stress fields. To predict future dynamical changes, it is necessary to account for this feedback and capture how ice rigidity changes over time in response to rift growth. If Larsen C retreats such that the compressive arch ceases to exist, it will resemble the pre-collapsed Larsen B ice shelf, producing widespread flow accelerations in response to the backstress loss from ice rises.

#### 1 Introduction

Ice shelves, as floating extensions of the grounded ice sheet, fringe ~75% of Antarctica’s coastline (Rignot et al., 2013). Ice shelves gain mass through ice flux from inland glaciers, local snow accumulation, and basal marine ice accretion, while they lose mass primarily via basal melting and iceberg calving (e.g., Depoorter et

al., 2013; Liu et al., 2015), together with minor runoff of surface meltwater (Bell et al., 2017). Although the direct effect of ice shelf mass loss on sea-level rise is negligible, ice shelves provide an important buttressing force to stabilize the grounded ice sheet and regulate the contribution from inland glaciers to global sea level (Dupont & Alley, 2005; Gagliardini et al., 2010; Gudmundsson, 2013; Pritchard et al., 2012; Reese et al., 2017; Thomas, 1979). Understanding the processes driving ice shelf retreat is therefore essential to generating realistic projections of future Antarctic ice sheet mass loss in a warming climate (DeConto et al., 2021; Noble et al., 2020; Pattyn & Morlighem, 2020).

Satellite data have indicated increasing trends in thinning and retreat of Antarctic ice shelves (e.g., Depoorter et al., 2013; Paolo et al., 2015), revealing the vulnerability of ice shelves to atmospheric warming and oceanic forcing (Holland et al., 2015; Liu et al., 2015; Vaughan & Doake, 1996). As a region sensitive to climate warming, the Antarctic Peninsula has undergone pronounced regional warming (Vaughan et al., 2003), along with rapid retreat of ice shelves and glaciers on both the west and east coasts (Cook et al., 2005; Doake & Vaughan, 1991; Rott et al., 1996; Scambos et al., 2009; Scambos et al., 2004). Successive retreat has occurred on the Larsen Ice Shelf along the east coast. The Larsen Ice Shelf was formerly composed of Larsen A, B, C, and D, four sections from north to south (Figure 1). Larsen A disintegrated in 1995, with an areal loss of  $\sim 1600 \text{ km}^2$  (Rott et al., 1996). Larsen B collapsed in February–March 2002, with an areal loss of  $\sim 3250 \text{ km}^2$  (Scambos et al., 2004). The rapid disintegrations of Larsen A and Larsen B triggered immediate flow accelerations of upstream glaciers (Rignot et al., 2004; Scambos et al., 2004), which highlights the importance of studying how an ice shelf evolves to an unstable condition and how ice shelf retreat affects upstream flow dynamics. This has also led to an increasing concern as to whether Larsen C will disintegrate in the future (e.g., Borstad et al., 2017; Glasser et al., 2009; Hogg & Gudmundsson, 2017; Jansen et al., 2010, 2015; Kulesa et al., 2014), especially after a giant iceberg (A68,  $\sim 5800 \text{ km}^2$ ) broke off from Larsen C in July 2017.

The disintegrations of Larsen A and Larsen B were preceded by warm air temperature and intense surface melt (Banwell et al., 2013; Scambos et al., 2003; Scambos et al., 2000). Meltwater-induced hydrofracturing has been postulated to be the dominant mechanism in the ice shelf collapse (van den Broeke, 2005; MacAyeal et al., 2003; Robel & Banwell, 2019), likely preconditioned by increased basal melting (Shepherd et al., 2003; Vieli et al., 2007). To predict the future stability of Larsen C, recent research has focused on surface melt and associated atmospheric drivers (Bevan et al., 2020; Luckman et al., 2014), and parallel efforts have focused on ocean-driven basal processes (Holland et al., 2015; Jansen et al., 2013; McGrath et al., 2014), such as basal melting and the stabilizing role of suture zones. Despite the importance of atmospheric and oceanic forcing, the stability of an ice shelf is also controlled by its stress field (Doake et al., 1998; Fürst et al., 2016; Kulesa et al., 2014; Lhermitte et al., 2020). The stress field, either compressive or tensile, is closely related to fracture opening. The spatial distribution and temporal evolution of fractures determine the ice shelf resilience, and enhanced fracturing along shear margins has been suggested to be critical for ice shelf stability and flow dynamics (Lhermitte et al., 2020; Joughin et al. 2008). Larsen A and Larsen B were already in an unstable stress state before their collapse as the front retreat had passed a “compressive arch” (Doake et al., 1998). Investigating the dynamic changes of ice shelves over the long term is important to understanding the destabilization processes. Multidecadal satellite observations on the retreat of Larsen C provide an excellent opportunity to study the long-term dynamic behavior of ice shelves and associated rifting and calving processes. Understanding these processes is also the key to predicting the future changes of other embayment-confined ice shelves, such as the Ross Ice Shelf and Filchner–Ronne Ice Shelf.

Here, we use multi-source satellite images spanning six decades and ice shelf modeling experiments to conduct a comprehensive analysis of the changes of ice shelf front, flow velocities, and stress fields over Larsen C. The earliest satellite imagery acquired in the 1960s allows us to extend the flow velocity data back to the 1960s–1980s. We analyze in detail the development of two rifts that led to the 2017 calving event, and reveal the close linkages between rift propagation, flow acceleration, and front retreat. We further carry out ice shelf modeling experiments to examine how ice shelf flow velocities and stress fields vary in response to the front geometry change due to ice shelf retreat and the mechanical weakening due to rift development.

## 2 Study area

Larsen C is confined by Jason Peninsula in the north and Kenyon Peninsula and Gipps Ice Rise in the south (Figure 1). Because of the barrier effect of the high mountain ridge on westerly winds, the east side of the Antarctic Peninsula is generally colder than the west side (King et al., 2017; Morris & Vaughan, 2003). However, strong downslope foehn winds occasionally bring warm and dry air masses over the northern Larsen C during the austral summer, causing intense surface melt in the northwest near the Cabinet Inlet (Elvidge et al., 2015; King et al., 2017). The structure of Larsen C (Figure 1) consists of fast flow units draining from the twelve inlets, and suture zones originating from the Churchill Peninsula, Cole Peninsula, Marmelon Point, Francis Island, Tonkin Island, and Joerg Peninsula (Borstad et al., 2017; Glasser et al., 2009). Suture zones connect those fast flow units and have been believed to play a significant role in stabilizing the ice shelf (Kulesa et al., 2014; McGrath et al., 2014). Two pinning points, the Bawden Ice Rise and Gipps Ice Rise, anchor the northern and southern ice front, respectively. The ice thickness varies from  $\sim 1000$  m near the grounding line to  $\sim 200$  m near the ice front.

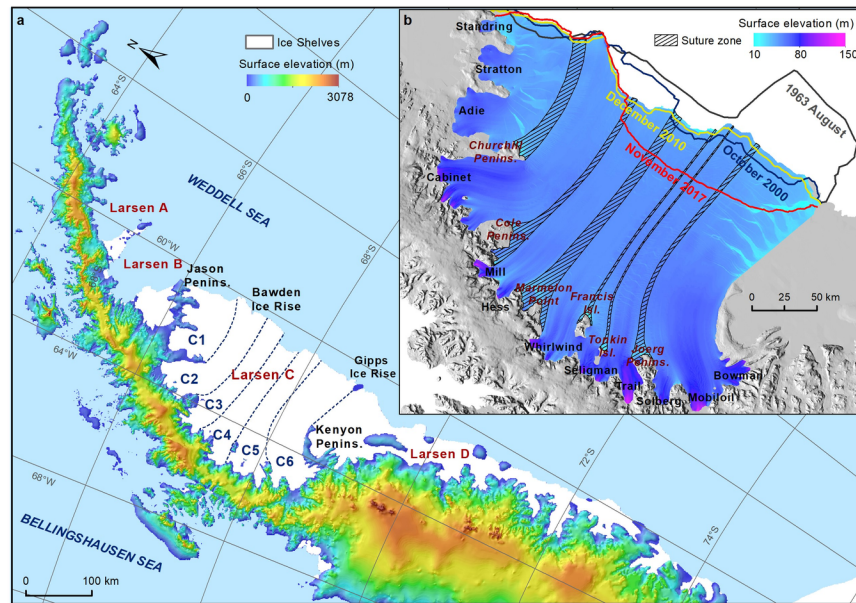


**Figure 1 .** Study area. **a .** Larsen Ice Shelf (A, B, C, and D) from north to south. The white area is the ice shelf extent in 2015. The color-coded area shows the surface topography of the grounded region. We divided Larsen C into six flow units (C1, C2, C3, C4, C5, and C6). **b .** The ice front locations in 1963, 2000, 2010, and 2017 with the ice shelf surface elevations from REMA DEM (Howat et al., 2019), twelve flow inlets, and suture zones flowing from peninsulas and islands.

## 3 Data and Methods

### 3.1 Mapping ice front, rifts, and flow velocities

We used multi-source satellite images acquired between 1963 and 2020 to map the ice front, identify rifts, and derive flow velocities in different time periods. The images include declassified intelligence satellite photographs (DISP) acquired by the ARGON mission, optical images acquired by the Landsat-4/5 TM, Landsat-7 ETM+, and Landsat-8 OLI sensors, and synthetic aperture radar (SAR) images acquired by the ERS-1, ERS-2, Radarsat-1, Envisat, and ALOS satellites. We performed image orthorectification, image co-registration, noise reduction, and image enhancement on the above set of images (Text S1).

We mapped the ice front locations of Larsen C for the period 1963 to 2020 (Figure S1) and delineated two

riffs in the vicinity of Gipps Ice Rise that were closely related to the 2017 calving event. We derived flow velocities over the ice shelf for multiple periods using an image-matching-based feature tracking method (e.g., Heid & Kääh, 2012; Liu et al., 2012; Scambos et al., 1992). The feature tracking method tracks the spatial displacements of moving and identical surface features from two sequential images acquired at different times. The derived flow velocity represents the average velocity between the acquisition dates of sequential images. The image-matching algorithm automatically searches for matching points between two images by maximizing the cross-correlation coefficient between conjugate areas in the two images. The cross-correlation-based method can achieve an accuracy of better than 0.5 pixel (Scambos et al., 1992). For our study, the image space was examined every 300 m to search for matching points, with a matching window of 64x64 pixels. Automated directional and local statistical filters (Liu et al., 2012) plus human inspection were employed to remove erroneous matches and verify the matching results. The accuracy of the derived velocity fields is determined by the image co-registration accuracy, image matching accuracy, and time separation of sequential images, which was estimated to be 3.7~25 m/year, depending on the image pairs used (Table S1).

### 3.2 Ice shelf modeling experiments

We used the Ice-sheet and Sea-level System Model (ISSM) (Larour et al., 2012) to conduct the ice shelf modeling experiments. We used the shallow shelf approximation (SSA) model (MacAyeal 1989; Weis et al. 1999; Morland 1987) to examine how ice shelf flow velocities and stress fields vary with front retreat and rift development (Text S2). For the model configuration, we used the anisotropic mesh adaptation method to generate the numerical mesh net nodes. The boundary condition was specified as kinematic for the interior ice shelf and dynamic for the ice shelf front. The flow law exponent  $n$  was set to 3. The ice rigidity  $B$  was initialized as  $1.5 \times 10^8 \text{ Pa s}^{1/3}$ . For the inversion of  $B$ , we used the M1QN3 optimization algorithm in ISSM (Morlighem et al., 2015) by minimizing a cost function defined as the weighted sum of the difference between the modeled and observed flow velocity fields and the gradient of the optimized  $B$  at each iteration. We further calculated the deviatoric stresses, including longitudinal deviatoric stresses and principal stresses (Text S1). We also calculated the backstress across the ice shelf. Backstress describes the stress transmitted upstream that opposes spreading of an ice shelf (Cuffey and Paterson, 2010), arising from side drag by lateral walls and slower flowing ice, and from basal resistance from grounded ice rises or ice rumples. These stress fields are tightly related to rift growth and ice shelf instability development.

## 4 Observations derived from satellite data

### 4.1 Retreat history of Larsen C during 1963–2020

During the period from August 1963 to March 2020 (Figure S1), the area of Larsen C decreased from 55,511 km<sup>2</sup> to 43,182 km<sup>2</sup>, a reduction of ~22%. In the six decades, Larsen C underwent two large retreat cycles, during 1976–1986, and during 2004–2017. Each cycle began with northern retreat near the Bawden Ice Rise (C1–C3 units), followed by southern retreat near the Gipps Ice Rise (C4–C6 units). For both cycles, the time interval between the northern and southern retreat was approximately ten years. In the first cycle, the northern retreat occurred at the C2–C3 units in 1976 due to a collision between an iceberg and the ice shelf (Ferrigno & Gould, 1987); afterwards, two large icebergs calved off from the C4–C6 units in 1986 (Skvarca, 1994), causing a retreat of ~100 km in the south. The ice shelf slowly advanced between 1986 and 2004. In the second cycle, the northern front detached from the C2–C3 units in 2004/2005, with an area loss of ~1500 km<sup>2</sup>. The major retreat of the southern front happened on 12 July 2017, when a ~5800-km<sup>2</sup> tabular iceberg detached from the C3–C6 units.

### 4.2 Rifting related to the 2017 calving event

The 2017 calving event resulted from the propagation of two rifts (labeled R1 and R2, Figure 2). Long and transverse fractures (Figure 2a) tend to form between Kenyon Peninsula and Gipps Ice Rise due to a stress condition change, where ice shelf flow becomes less constrained by the lateral shear margins after passing by Kenyon Peninsula. The majority of the fractures terminate near the Joerg suture zone (Figure 2a). Suture zones can inhibit fracture growth because of the material properties of marine ice underneath (Kulesa et

al., 2014, 2019; McGrath et al., 2014). The rift R1, a transverse rift propagating perpendicular to the flow direction, developed from a preexisting fracture (L1 in Figure 2a) that is identifiable on the 1963 DISP imagery. The lateral extent of R1 changed little until 2008, when it began to propagate towards R2. By 2010, the southern rift tip of R1 had traveled ~14 km from its 2006 location (from A' to A, Figure 2c), to a point less than 1 km from R2. At the northern end, R1 developed a new rift trajectory from point B' to B (Figure 2c), and subsequently propagated to the north along this trajectory. R2 was an oblique rift that formed between Gipps Ice Rise and a transverse fracture (L2 in Figure 2a). R2 is not present on the 1963 DISP imagery. Its formation was very likely due to the front geometry change caused by the 1986 retreat. R2 widened over time, while its rift tips exhibited little change until 2013. Then, it began developing towards the south, and the rift tip almost reached Gipps Ice Rise (Figure 2e). Simultaneously, R1 penetrated through the Joerg suture zone and started rapid propagation to the north (Figure 2d). R1 cut through the C5 unit in 2014 and had propagated across the Tonkin suture zone by January 2016 (Figure 2d). By March 2017, the length of R1 dramatically increased by ~65 km, and its northern rift tip ('B') reached the Cole Peninsula suture zone (connecting the C2 and C3 units). R1 continued penetrating through the Cole Peninsula suture zone, but did not extend into the C2 unit. Instead, it was developing along the C2 unit boundary towards the ice front, resulting in the complete detachment of the downstream portion in July 2017.

The propagation of R1 appears to have had a strong association with the development of R2. The extension of R2 to Gipps Ice Rise was immediately followed by the rapid growth of R1 towards the north. This suggests that rifting can promote the growth of another rift by weakening the lateral shear margins near an ice rise. Ice rises are locally grounded topographic highs in ice shelves. They often act as pinning points, buttress upstream ice flows and play an active role in ice shelf stability (Favier & Pattyn, 2015; Matsuoka et al., 2015). Weakening around ice rises could reduce their buttressing effect, leading to enhanced longitudinal stretching and creating favorable conditions for rift propagation. We further explore this hypothesis through modeling experiments in Section 5.

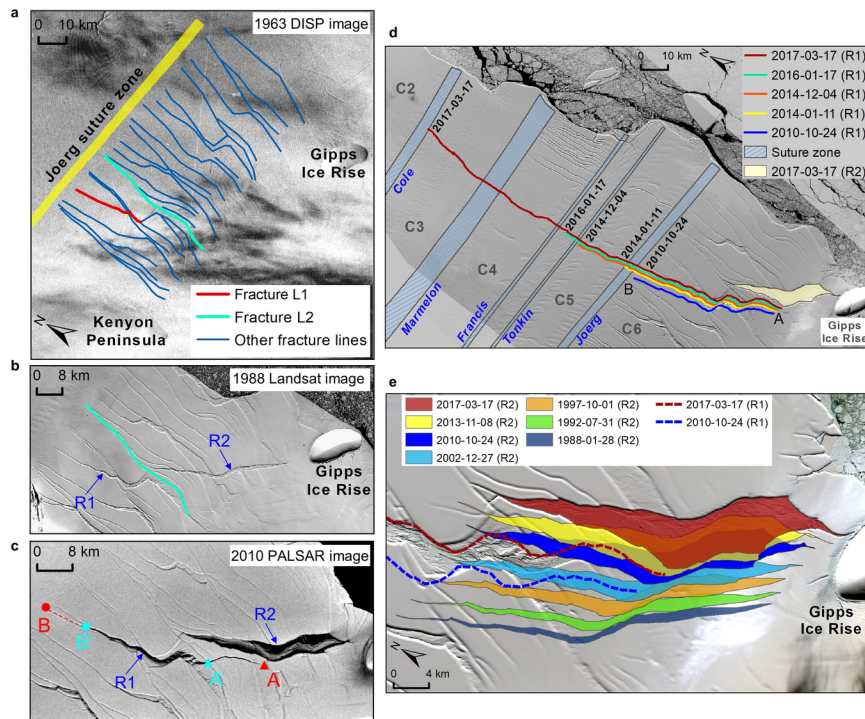


**Figure 2** . Development of two rifts that led to the 2017 calving event. **a** . Long and transverse fractures

formed between Kenyon Peninsula and Gipps Ice Rise, delineated from the 1963 DISP imagery. **b** . The locations of R1 and R2 on the 1988 Landsat imagery. The cyan line corresponds to L2 in panel **a** . **c** . The locations of R1 and R2 on the 2010 PALSAR imagery, showing the widening of R2 and the propagation of R1 (from points A' to A and B' to B). **d** . The propagation of R1 from 2010 to 2017. **e** . The widening of R2 between 1988 and 2017 following the 1986 calving event that occurred at the southern ice front.

#### 4.3 Temporal variability of flow velocity during 1963–2020

The earliest flow velocities were derived from the 1963 DISP imagery and the Landsat imagery acquired in 1986 and 1988. Since the available images for 1986 cannot fully cover Larsen C, we used the 1988 imagery to fill the data gaps. We also derived the 1986–1988 flow velocities for the area where both 1986 and 1988 images are available. Due to the limited resolution of the DISP imagery and the long-time span with the Landsat data, the flow velocities for this period (1963–1986/1988) are relatively sparse, and are distributed over the areas with large visible surface features (Figure 3a). Nevertheless, these velocity measurements still provide important baseline information for examining the long-term changes in ice flow. Figure 3b shows the temporal variability of flow velocity over five areas, including the upstream ice shelf (Area 1), the northern downstream portion (Area 2), the ice front near Bawden Ice Rise (Area 3), the central ice shelf (Area 4), and the southern downstream portion (Area 5). Before 1990, there was no significant velocity change across Larsen C. On average, the flow velocities after 2000 were higher compared to the velocities before 1990. Area 1 shows a gradual velocity increase between 2000 and 2016. Both Area 3 and Area 5 exhibit a step change in velocity ( $\sim 50$  m/year) between the 2000–2002 and 2008–2010 periods. The acceleration of Area 3 was related to the northern calving near Bawden Ice Rise in 2004/2005. The acceleration of Area 5 was concurrent with the rift propagation of R1 during 2006–2010. The 2017 calving event did not trigger an immediate flow speedup across the ice shelf.

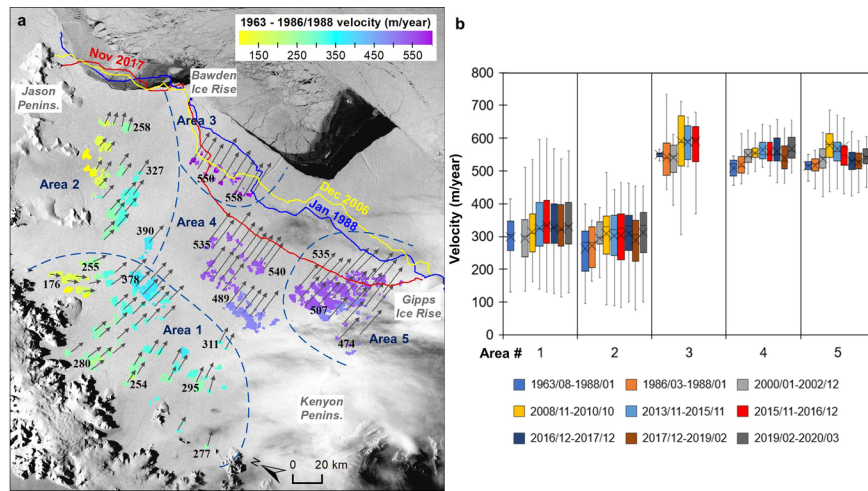


**Figure 3** . **a** . The 1963–1986/1988 flow velocities. The background image is the georeferenced DISP image showing the extended ice front in the south in 1963. The dashed lines divide the velocity data into five regions (Areas 1–5). **b** . Box and Whiskers plots of the time-series flow velocities for the five areas, generated based on the velocity measurements of the locations where the 1963–1986/1988 velocity data are available for each period. The “x” markers indicate the mean value.

#### 4.4 Flow accelerations associated with rifting and calving

The most significant velocity change was strongly related to the rift development within the downstream portion of the C5–C6 units (Figure 4). There was a sharp velocity change along the rift line during 2015–2016 (Figure 4e) immediately before the calving occurred. Along the C6 flow line (Figure 4h), the average velocity of the portion that calved in 2017 increased by more than 50% from  $570 \pm 16$  m/year during 1986–1988 to

890±36 m/year during 2015–2016. The largest increase over this period was between 2013–2015 and 2015–2016, when the velocity increased by 21.6±2.5% from a speed value of 731±25 m/year. In comparison, the central ice shelf (C4; Figure 4g) exhibited much less variability in velocity before calving. The calved portion of C4 had an average velocity of 723±21 m/year during 2015–2016, increasing by only 3.1±0.7% relative to the previous period 2013–2015. However, there was a velocity increase of 9.1±2.3% between 1986–1988 and 2000–2002 from the ice front to an upstream distance of ~80 km. This acceleration was very likely due to the velocity adjustment in response to the front geometry change caused by the 1986 retreat. Despite the sparse velocity data before 2000, this observed acceleration pattern may indicate a lagged response of flow velocity to front retreat. The lagged response suggests that although the 2017 calving event has not yet induced any significant flow accelerations, there is potential for a future flow velocity response to the 2017 event.

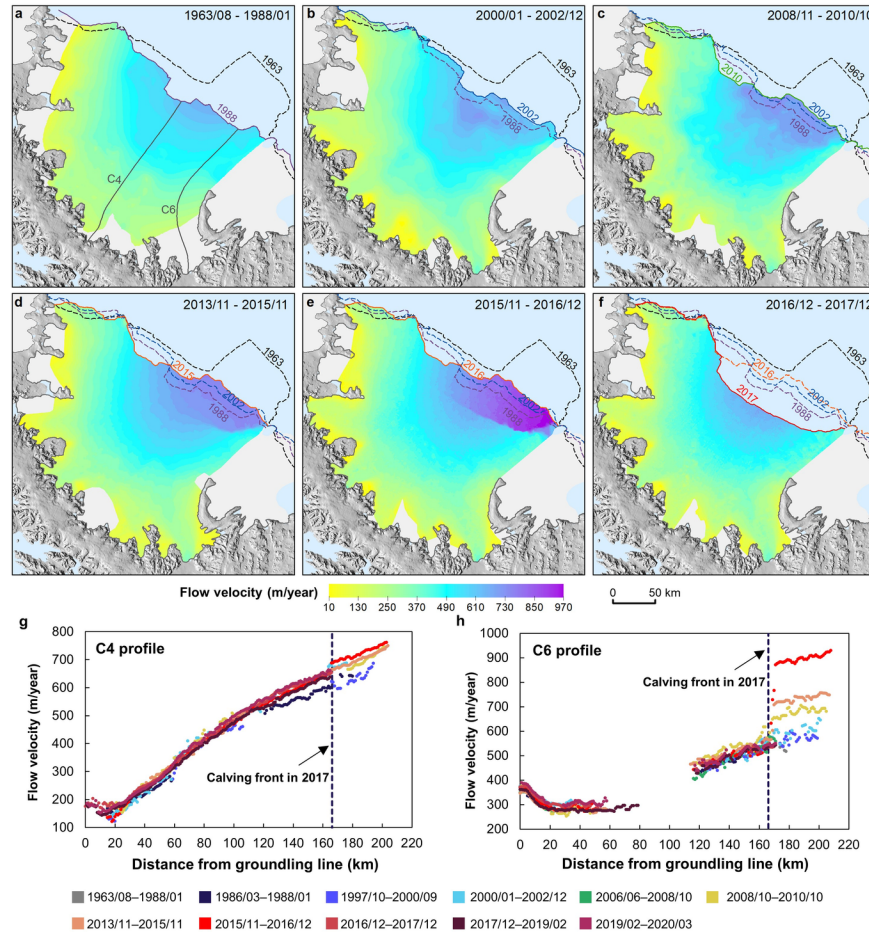


**Figure 4 .** Flow velocity maps (a–f) of six selected periods with ice front changes, and along-flow velocity profiles for C4 (g) and C6 (h). The locations of the C4 and C6 centerlines are shown in panel a .

## 5 Modeling experiments

The observational data have indicated a clear but also complex linkage between ice shelf retreat, flow acceleration, and rift development. Both front geometry change and rift development modulate the stress conditions across the ice shelf, which in turn change flow velocities and strain rates, further affecting rifting and calving. We conducted diagnostic modeling experiments to investigate how varying front geometry and rift-induced weakening control the dynamic responses of ice shelf flow velocities and stress fields.

## 5.1 Ice rigidity inversion and modeling scenarios

Before the diagnostic experiments, we first solved for the ice rigidity  $B$  using the inversion procedure in ISSM. We used the 450-m resolution MEaSUREs phase-based Antarctica ice velocity data product (Mouginot et al., 2019) to solve for  $B$ . We used this velocity product to avoid uncertainties induced by velocity interpolation errors. This velocity product agrees best with the derived 2008–2010 flow velocities, with an average difference of  $10 \pm 25$  m/year. Figure 5a shows the optimized ice rigidity  $B$ . This parameter defines the relationship between strain rate and stress, and is affected by ice temperature, fabric, water content, impurities and presence of cracks. Low values of  $B$  indicate “soft” ice and high values indicate “stiff” ice. The spatial pattern of  $B$  (Figure 5a) shows a good agreement with the suture zones and the zones of rapid shearing where outlet glaciers are flowing past promontories near the upglacier end of the ice shelf. The low values of  $B$  near Gipps Ice Rise (highlighted area in Figure 5a) are due to the observed rift that mechanically weakened the ice shelf, thus making the ice appear “softer” than the surrounding ice. This results from the objective of parameter inversion, which is to minimize the difference between modeled and observed flow velocities under the continuum-mechanical modeling framework. When simulating for the years without rifting, these low values of  $B$  derived from the rifted condition could artificially influence the model simulations. We modified the  $B$  values in this rifted area (Figures 5b and c) for different modeling scenarios. We considered three scenarios as follows.

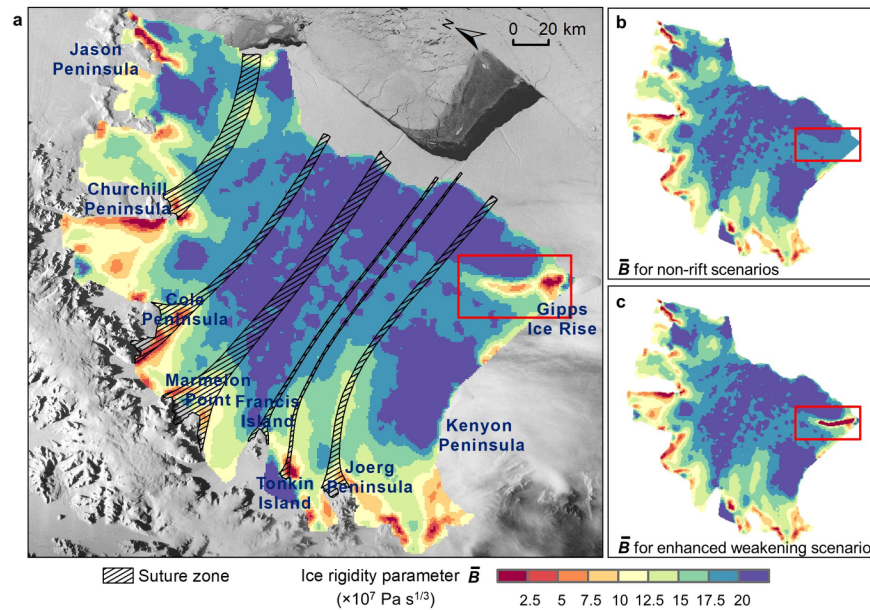


**Figure 5 . a .** The optimized ice rigidity  $B$  through inversion in ISSM. **b .** The modified  $B$  used for the non-rift scenario. **b .** The modified  $B$  used for the enhanced weakening scenario.

**Non-rift scenario with different front geometry conditions.** This scenario aims to examine the dynamic responses of ice shelf velocity and stress to front geometry change. We controlled for rift effects by replacing the low values of  $B$  near Gipps Ice Rise with the values of the adjacent intact areas (Figure 5b). We tested nine front geometry conditions (Figure 6), including four historical front locations (F1–F4), and five hypothetical front locations (H1–H5) under future retreat scenarios. H1–H5 were determined by assuming a radical retreat scenario, in which the new ice front reaches the compressive arch. The compressive arch is the boundary where the second principal stress changes from negative to positive, and has been used as a critical boundary to predict ice shelf instability (Doake et al., 1998; Kulesa et al., 2014). It has been suggested

that ice shelf retreat will become irreversible once the ice front retreats behind the compressive arch. H1 (Figure 6e) is the front location where the retreat reaches the current compressive arch (shown in Figure 6d); H2 is the front location where the retreat reaches the compressive arch for the geometry condition H1, and similarly for H3. Once the ice front reaches H3 or exceeds H3, the compressive arch would no longer exist. H4 is the front condition if the H3 front continues retreating another 1 km, and H5 is the front condition if H4 keeps retreating by  $\sim 20$  km (Figure 6g). H4 and H5 were used to test how sensitive the ice shelf would be to changes in the ice shelf front when the compressive arch is absent.

**Rift-scenario 1 with original  $B$ .** Through two rift scenarios, we aim to test the hypothesis based on the observations: the weakening due to the rift R2 was crucial for the propagation of R1, which resulted in the 2017 calving event. In this scenario, we used the original ice rigidity  $B$  (Figure 5a), which includes, to a certain extent, the R2-induced weakening.

**Rift-scenario 2 with enhanced weakening.** We considered a weakening-enhanced scenario by further decreasing the rigidity  $B$  to a minimum value of  $0.1 \times 10^8 \text{ Pa s}^{1/3}$  over the rifted area (Figure 5c).

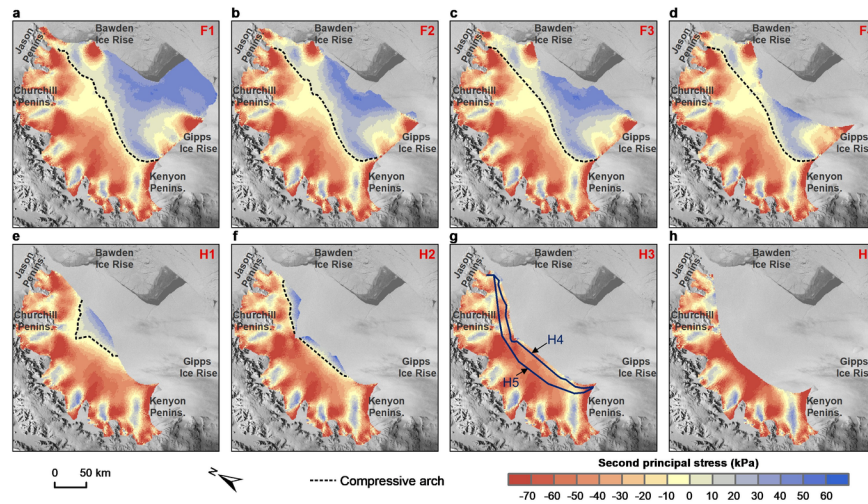


**Figure 6 .** Second principal stresses and compressive arch locations for different front geometry conditions (non-rift scenario). F1–F4 are the front locations in 1963, 2000, 2013, and 2017, respectively. H1–H5 are the hypothetical front locations under future retreat scenarios.

## 5.2 Dynamic responses to front retreat (non-rift scenario)

The retreat events during 1963–2020 neither exceeded nor modified the compressive arch (Figures 6a–d). Under future retreat scenarios, successive retreat would allow the compressive arch to migrate upstream until H3 (Figures 6e, f). The front geometry change due to retreat can result in flow accelerations and backstress loss (Figure 7), with the magnitude and extent depending on the location of the retreat. The two retreat cycles reduced the backstress at the areas adjacent to the ice rises and the central downstream portion (Figure 7i–k). Flow accelerations (greater than 20 m/year) caused by front geometry change are limited to the central downstream portion and are less than 50 m/year for the majority of Larsen C (Figures 7a–c). Therefore, the front geometry change due to the past retreat events is insufficient by itself to explain the observed velocity increase. We compared the derived flow velocities with the modeled flow velocities of corresponding front geometry. Over the downstream portion of the ice shelf, the averaged difference increases over time with the propagation of R1 and R2 from  $9.8 \pm 8.5\%$  (2000–2002, F2 condition), to  $16.3 \pm 8.6\%$  (2008–2010, F3 condition), to  $17 \pm 12.9\%$  (2013–2015, F3 condition), and to  $23.4 \pm 24.5\%$  (2015–2016, F3 condition). This suggests that, to make a realistic prediction of flow velocity change due to ice shelf retreat, it is necessary to

first consider rift development in response to front retreat. Nevertheless, the modeling scenario considering only the front geometry condition can be used with the observational data as a diagnostic indicator. The increasing difference between observed and modeled flow velocities over time may be an indicator for future calving events.

However, even without considering rifts, once the ice front reaches the current compressive arch, widespread flow accelerations ( $\sim 25\%$ ) would be triggered (Figure 7d), as a result of the dramatic backstress loss (Figure 7l) from Bawden Ice Rise and Gipps Ice Rise. This emphasizes the important role of ice rises in stabilizing the ice shelf. Complete buttressing loss from ice rises would cause ice-shelf-wide flow accelerations, and the backstress-reducing effect would extend to the grounding line. After the compressive arch ceases to exist, even small perturbations in the ice front would cause large-scale backstress loss and flow accelerations (Figures 7g–h, o–p), particularly over the C2 and C6 units. This effect would reach the grounding line, and the upstream glaciers feeding the C2 and C6 units would speed up in response to the buttressing loss caused by a small retreat at the ice front. This scenario resembles the pre-collapsed Larsen B, for which the compressive arch was removed and flow accelerations occurred across the ice shelf. These modeling experiments suggest that ice rises are crucial for determining the tipping point of ice shelf stability. The compressive arch is the critical boundary, beyond which the ice shelf flow velocities and stresses are highly sensitive to front retreat. Once the compressive arch is absent, front geometry change will become an important control on ice shelf flow dynamics and stress conditions.

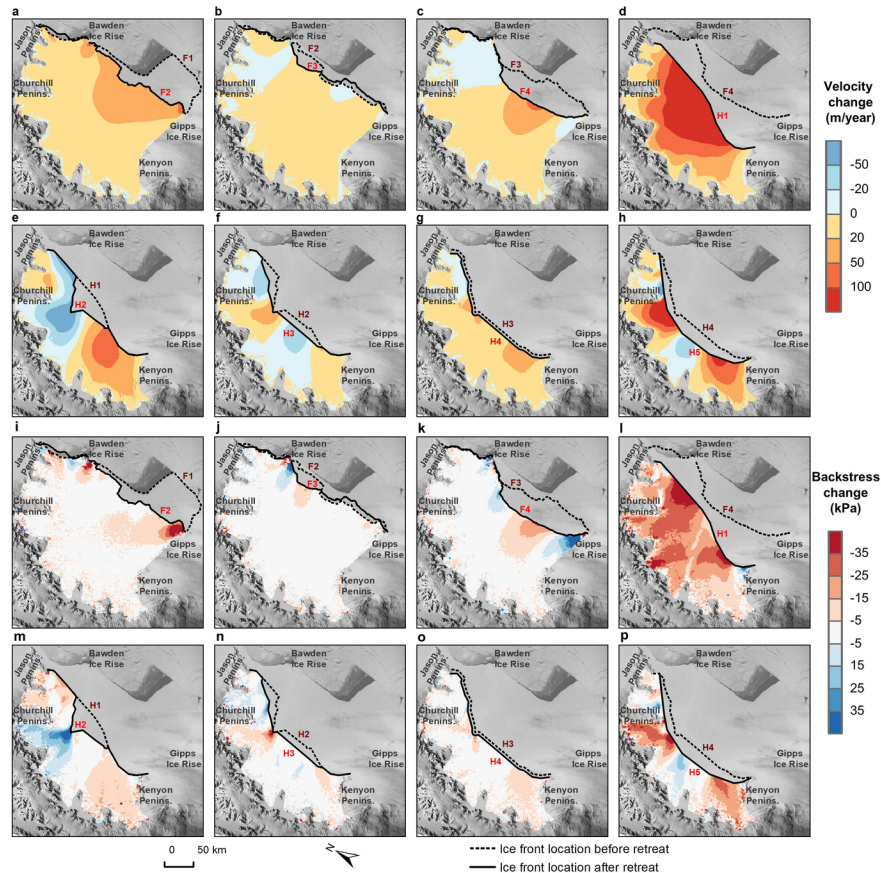


**Figure 7** . Changes of modeled flow velocities (a–h) and backstresses (i–p) in response to the front geometry changes (non-rift scenario).

### 5.3 Longitudinal deviatoric stress field and rift opening (non-rift scenario)

We find that the modeling scenario considering only the front geometry condition is also useful to diagnostically predict the rift opening location. Figures 8a–b show the longitudinal deviatoric stress fields for F2 (2000 front) and F3 (2013 front), with positive values representing tensile conditions along the flow direction and negative values for compressive conditions. The locations where rifts opened strongly coincided with the transitional zone from compressive to tensile longitudinal conditions, including the rift near Bawden Ice Rise (Figure 8c) that caused the northern calving event in 2004/2005, and the rift R2 (Figure 8d) whose expansion to Gipps Ice Rise directly related to the rift R1 and eventually caused the 2017 calving event. This transitional pattern appears to be a characteristic feature near ice rises. Although we did not account for the rift-induced weakening effect on ice rigidity, the longitudinal deviatoric stress field may be used as an important diagnostic feature to identify potentially vulnerable areas that are favorable for rift opening, especially within the transitional zone from compressive to tensile conditions. Identifying the potential locations of the initial rift opening is a necessary step for introducing rift-caused damage into ice shelf models.

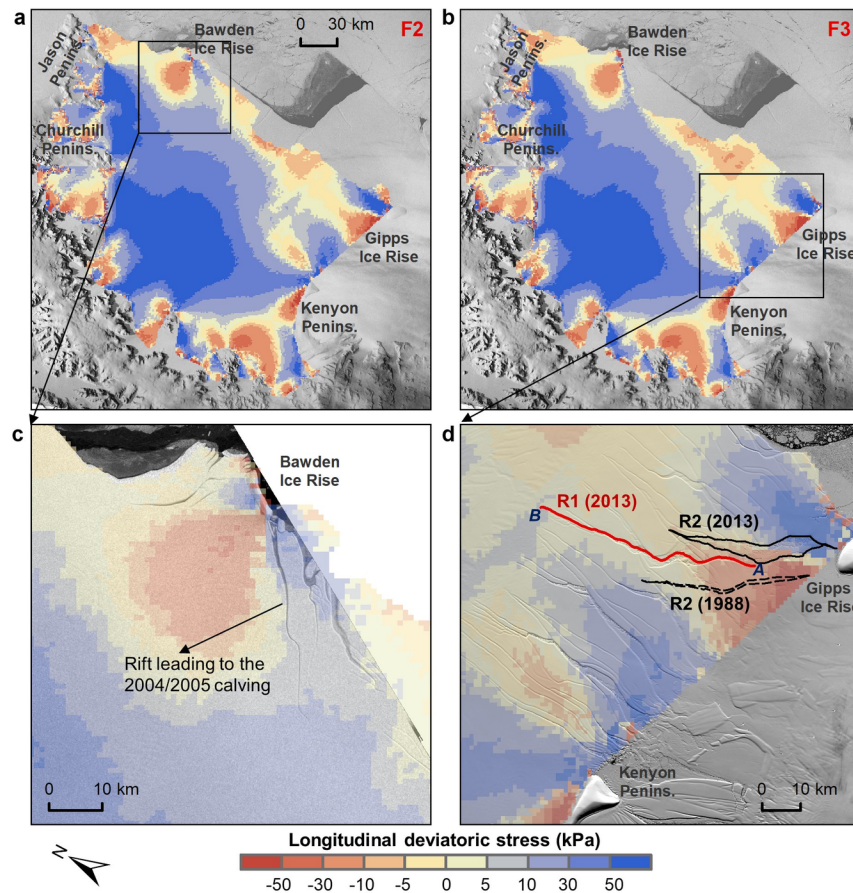


**Figure 8** . Longitudinal deviatoric stress fields for geometry conditions F2 (panels a and c , ice front in 2000) and F3 (panels b and d , ice front in 2013). The background image in panel c is the Envisat ASAR image acquired on August 03, 2004, showing the rift causing the northern calving event. The background image in panel d is the Landsat-8 OLI panchromatic image acquired on January 11, 2014, showing the expansion of R2 to Gipps Ice Rise.

#### 5.4 Impact of rift-induced weakening (rift scenarios)

The modeling results of rift scenarios indicate the R2-induced weakening near Gipps Ice Rise was critical to the propagation of R1. If the weakening effect of R2 is not considered, the southern rift tip (‘A’) of R1 would

be in a compressive longitudinal condition (Figure 8d). Once the R2-induced weakening is incorporated (Figure 9b), the southern rift tip ('A') would be in a tensile longitudinal condition that is favorable for rift growth. This suggests that R1 would be less likely to propagate towards the south if the ice shelf were not damaged by R2 near the ice rise. Based on satellite images, R1 almost reached R2 in 2010 (Figure 2c), which further weakened the area. The continued weakening can further enhance the longitudinal stretching over an expanded area for both rift scenarios (Figures 9e, h), indicating that this weakening could promote the subsequent northward propagation of R1.

We also analyzed the first principal stresses (Figure 10). The first principal stress is the maximum value of stress that is normal to the plane in which the shear stress is zero. Therefore, it indicates the magnitude and orientation of the maximum tensile stress. Fractures tend to open along the direction of the first principal stress, and the opening rate would be maximized if the flow direction is along the first principal axis (e.g., Benn et al., 2007; Colgan et al., 2016; Kulesa et al., 2014). The angle between the first principal axis and flow direction (stress-flow angle) can be used to evaluate rift propagation and ice shelf stability (Kulesa et al., 2014). A small stress-flow angle would be more likely to promote rift propagation than a large angle. The rift-induced weakening would modify the stress-flow angles (Figures 10a-c) along the trajectory of R1 to more favorable conditions for rift propagation. The magnitude of first principal stresses would also increase in response to the rift-induced weakening (Figure 10d-f). The northern rift tip ('B') of R1 reached an area with stress-flow angles of less than 10 degrees after January 2016, which could explain the rapid propagation of R1 afterwards. The path of rift tip 'B' growth was perpendicular to the flow direction. Once the rift tip was in the area where the first principal axis was aligned with the flow direction, the rift growth was unstoppable until it reached to the area where the stress-flow angles were greater than 30 degrees. Therefore, the rift-induced weakening could increase both longitudinal stresses and first principal stresses and modify the stress-flow angles nearby, resulting in favorable stress conditions for the rift (R1) propagation towards the north. The opening of R2 therefore preconditioned the R1 growth and the 2017 calving event.

The modeling results also indicate the rift-induced weakening caused the localized flow accelerations at the downstream portion of southern Larsen C. The flow velocity increases near Gipps Ice Rise as compared to the non-rift scenario are shown in Figure 9d. With the further enhanced weakening, the acceleration increases both upstream and downstream of the rifted location (Figure 9g). This is consistent with the observed spatial pattern of velocity increase (Figure 4). The rift development can also reduce the ice shelf backstress (Figures 9c, f, i), although the magnitude and extent of backstress loss depend on how much weakening is caused by rifts. With enhanced weakening, the backstress loss can extend upstream and potentially reach the grounding line. This suggests that rift propagation needs to be considered for evaluating the buttressing change of ice shelves.

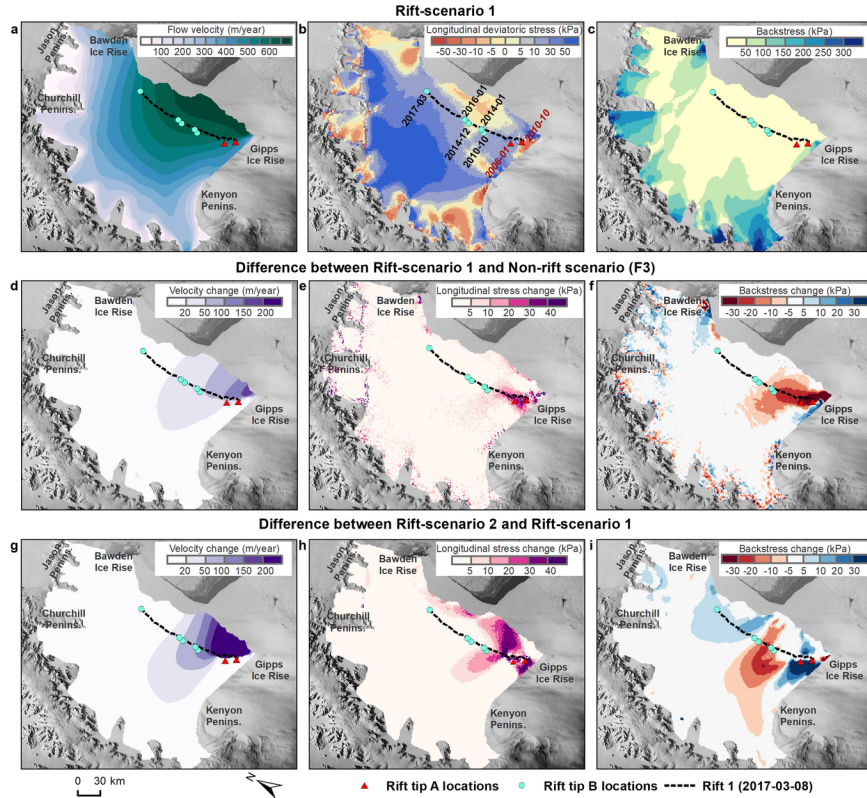


**Figure 9** . Modeled flow velocity (a ), longitudinal deviatoric stress (b ), and backstress (c ) for rift-scenario 1. Differences of these quantities between rift-scenario 1 and non-rift scenario (d –f ), and between rift-scenario 2 and rift-scenario 1 (g –i ).

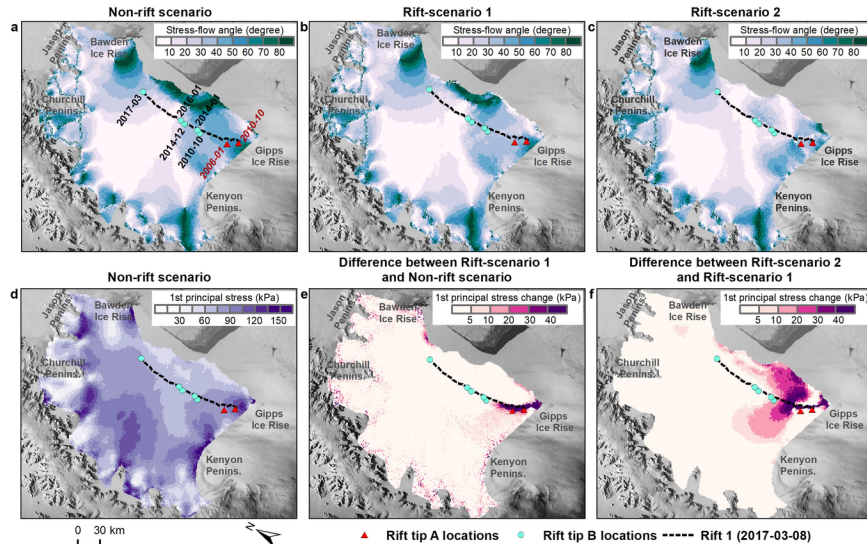


**Figure 10** . Stress-flow angles for non-rift scenario (a ), rift-scenario 1 (b ), and rift-scenario 2 (c , enhanced weakening). First principal stress field for non-rift scenario (d ), and differences between rift-scenario 1 and

non-rift scenario (e), and between rift-scenario 2 and rift-scenario 1 (f). The extent of R1 is shown (dashed line) with the rift tip locations between 2006 and 2017.

## 6 Discussion

The multidecadal satellite data and modeling experiments indicate the primary role of rifting processes in controlling the retreat of Larsen C over the past six decades. The two retreat cycles were characterized by tabular iceberg calving due to rift propagation. The rifts leading to calving developed near the Bawden Ice Rise in the north and the Gipps Ice Rise in the south. The time series of satellite data allowed us to analyze the rifting processes causing the 2017 calving event in a high level of detail. The 2017 calving event resulted from the propagation of two rifts, including a transverse rift (R1) formed downstream of Kenyon Peninsula and an oblique rift (R2) formed near Gipps Ice Rise. The observed flow accelerations were mainly related to the propagation of these two rifts. Enhanced weakening due to R2 near Gipps Ice Rise increased both longitudinal and first principal stresses around R1, and modified the stress-flow angles, creating favorable conditions for the northward propagation of R1. This indicates the importance of considering feedbacks between different rifts. Several studies (e.g., Borstad et al., 2017; Jansen et al., 2015) discussed the rift development causing the 2017 calving event, but treated R1 and R2 as one single rift and mainly focused on the northward propagation. Our results suggest that the southward propagation of both R1 and R2 preconditioned the northward propagation.

According to linear elastic fracture mechanics (LEFM), a fracture propagates when the stress intensity factor at a crack tip exceeds the material fracture toughness (Hulbe et al., 2010; Lipovsky, 2020). At the fracture tip, the stress intensity factor is determined by fracture geometry, fracture length, and stress field. The stress intensity factor has three modes: Mode I—opening (tensile), Mode II—sliding (in-plane shear), and Mode III—tearing (antiplane shear). The propagation of R1 was dominated by Mode I. Fracture propagation continues until the stress intensity factor is less than the fracture toughness. Suture zones are suggested to have resistive effect on rift propagation because of the high fracture toughness of marine ice underneath (Borstad et al., 2017; Kulesa et al., 2019; McGrath et al., 2014). Marine ice has different material properties from meteoric ice originating from glacial ice, and was detected underneath the Larsen C suture zones (Holland et al., 2009; Jansen et al., 2013). Assuming that the spatial distribution of fracture toughness is fixed, the increased tensile stresses at the crack tips of R1 are necessary conditions to activate the propagation of R1. The modeling results indicate the R2-induced weakening near Gipps Ice Rise caused the enhanced tensile stresses around R1, highlighting the importance of rift features around ice rises. Meanwhile, reduced fracture toughness of suture zones due to ice shelf thinning should also be considered. Widespread thinning has been observed over Antarctic ice shelves from satellite altimetry data (Adusumilli et al., 2020), including Larsen C (Adusumilli et al., 2018; Shepherd et al., 2003). The surface lowering of Larsen C has been attributed to multiple factors, including firn compaction, ice divergence due to flow acceleration, and basal melt (Holland et al., 2015; Shepherd et al., 2003). A high basal melt rate was observed near Bawden Ice Rise (Adusumilli et al., 2018). Ocean-driven melting underneath Larsen C can enhance the rifting processes by 1) reducing marine ice underneath the suture zones, decreasing the fracture toughness of suture zones; 2) destabilizing the ice rises and reducing the buttressing force from ice rises (Borstad et al., 2013); and 3) thinning and weakening shear margins (Alley et al., 2019; Dow et al., 2018; Lhermitte et al., 2020).

To better predict ice shelf retreat due to rifts, we not only need to know whether a rift would propagate until calving occurs, but also where rifts tend to initiate. Rifts initiate at preexisting cracks or flaws (Hulbe et al., 2010). A recent study based on ICESat-2 data (Wang et al., 2021) found that the vertical depth of preexisting fracture features is critical for predicting rift locations. Theoretical modeling studies (e.g., Lipovsky 2020) suggest that the loss of marginal strength, when ice flows out of an embayment, can trigger rift growth. Our modeling results (Figure 8) suggest that the transitional area from a compressive (longitudinal) condition to a tensile (longitudinal) condition resulting from ice shelf geometry conditions is also a potential location for rift initiation and opening. There were three such transitional areas at the downstream portion of Larsen C, including the area near Bawden Ice Rise, the area near Gipps Ice Rise, and the area downstream of Kenyon Peninsula. Satellite images showed that the rifts causing the northern and southern calving events

were initiated in these areas. The area downstream of Kenyon Peninsula is a typical transitional area from strong to weak shear margins, consistent with the modeling study of Lipovsky (2020). The transitional areas can be identified through diagnostic modeling given a front geometry condition without considering ice shelf damage. Once a rift is initiated, the rift-induced weakening must be incorporated to examine whether the rift will propagate in response to the modification of stress field. The weakening is enhanced when the rift growth continues, further altering the stress field. Therefore, it is important to capture the time-varying effect of rifts on ice rigidity in ice flow models. Capturing such feedbacks appears to be essential for modeling flow velocity fields and subsequent rift propagation. Continuum damage mechanics (Borstad et al., 2012, 2013; Krug et al., 2014) have been recently utilized to incorporate fracture-induced weakening into a viscous continuum damage model. The damage factor is a scalar variable that is quantified by an inversion (ice rigidity) approach. In this case, damage-related flow velocities are required to invert for the damage factor. Further investigation into the temporal evolution of rift length and associated damage is needed to enable parameterization of these processes within a modeling framework.

The velocity data indicate that the impact of the 2017 calving event is limited on the ice shelf flow dynamics. The calved portion was located in the “passive ice” zone (Fürst et al., 2016; Reese et al., 2017), where the front retreat has little effect on ice shelf buttressing. We observed flow accelerations in the central ice shelf after 2000, which might be a velocity adjustment to the front geometry change resulting from the calving events before 1990. The modeling experiments (Figures 7c, 7k) show the front geometry change due to the 2017 calving would increase the velocity (although at a low magnitude) and decrease the backstress in the central ice shelf, suggesting a potential time-lag between front retreat and ice shelf flow acceleration. If the retreat continues and the ice front reaches the compressive arch, widespread flow accelerations will be triggered due to front retreat. The observed flow accelerations were mainly caused by the rift development in the south. To predict future ice shelf flow dynamics due to front retreat, rift initiation and propagation and associated weakening effect on ice rigidity should be considered for modeling flow velocity fields.

Following the disintegration of Larsen A and Larsen B, one pressing question is whether Larsen C will disintegrate in the same manner. The collapses of Larsen A and Larsen B were preceded by extensive surface melt, and hydrofracturing has been the prevailing hypothesis for explaining the ice shelf collapse (e.g., van den Broeke, 2005; MacAyeal et al., 2003). Abundant meltwater, surface fractures, and favorable stress conditions are the necessary elements of hydrofracturing. Lai et al. (2020) applied LEFM and assessed the vulnerability to hydrofracturing across all Antarctic ice shelves, in which Larsen C was classified as vulnerable to hydrofracturing. However, it is still questionable whether there will be sufficient meltwater to fill the crevasses on Larsen C. Although several studies indicated that foehn wind enhances the surface melt rate over Larsen C (Datta et al., 2019; Elvidge et al., 2020; King et al., 2017), the extent of ponded water is limited in space, mostly occurring at the northern upstream portion at the Cabinet Inlet (C3 unit). Besides excessive melt occurred on Larsen A and Larsen B, their pre-collapse front geometries were already in unstable conditions after the compressive arch was reached (Doake et al., 1998). Larsen C will resemble the pre-collapse Larsen B if the front geometry reaches the position of H3 and the compressive arch is absent (Figure 6). The disintegration of Larsen C is less likely to occur in the current condition. However, given the importance of rifting processes to the stability of Larsen C, it is critical to monitor how atmospheric warming and oceanic forcing will affect rifting processes in the future.

## 7 Conclusions

We combined multi-source satellite data over the past six decades to investigate changes occurring over the Larsen C ice shelf. The total ice shelf area was reduced by more than 20% from 1963 to 2020, as a result of two large retreat cycles. Each cycle was characterized by a northern retreat near Bawden Ice Rise followed by a southern retreat near Gipps Ice Rise, in which rifting-induced tabular iceberg calving was the dominant mechanism. We analyzed the temporal evolutions of two rifts that caused the 2017 calving event in the south, and found their close interactions in weakening the ice shelf. In particular, the weakening due to R2 near Gipps Ice Rise preconditioned the rapid propagation of the major rift R1. We observed a lagged response of flow acceleration to front retreat, which leads to our conjecture that there will be a gradual velocity increase

in response to the 2017 calving event, despite relatively small recent changes. The ice shelf retreat away from pinning points (ice rises) to the location of compressive arch will reduce the ice shelf backstress and lead to widespread flow accelerations. When the compressive arch ceases to exist, small retreat events can trigger large-scale backstress loss and flow accelerations extending to the upstream glaciers.

The results of this study in combination with observations of the pre-collapsed Larsen B suggest a chronology of ice shelf destabilization processes for embayment-confined ice shelves. Rifts initiate at preexisting cracks and/or areas with favorable stress conditions, such as the transitional area from compressive to tensile longitudinal conditions. Ice rises and locations with a transition from strong lateral shear margins to weak margins (e.g., occurring near an island or peninsula) generally have such characteristic stress patterns. Rifts would propagate at these transition areas, if the stress intensity at the crack tips exceeds the fracture toughness. Rift growth leads to mechanical weakening of ice and a change in ice rigidity property. The weakening, particularly near ice rises and/or shear margins, results in flow accelerations, further modifies the stress field by increasing longitudinal stretching and decreasing stress-flow angles, hence creates more favorable conditions for rift propagation, and eventually causes ice front retreat. If the front retreat occurs within the “passive ice” area and does not extend to the compressive arch, a limited or lagged response in flow velocity and stress field would be triggered. If the front retreats behind the compressive arch, widespread flow accelerations and backstress loss would be triggered, causing dynamic thinning and stress field change across the ice shelf. The compressive arch location may move further upstream or become fully absent. The absence of a compressive arch would create an unstable front condition, followed by persistent front retreat. If surface melting and ponding are prevalent due to atmospheric warming, hydrofracturing can destabilize the ice shelf rapidly. Oceanic forcing can affect this process by thinning shear margins and reducing marine ice underneath suture zones, both of which lower the fracture toughness and therefore enhance weakening and fracturing. Our results emphasize the need for capturing key processes in ice shelf evolution models. In particular, the response of the ice shelf mechanical strength to the presence of rifts and the feedbacks that can accelerate ice shelf retreat need to be incorporated in the models.

## Acknowledgments

This research was supported in part by a Seed Grant award from the Institute for Computational and Data Sciences at the Pennsylvania State University. Part of the work was supported by the University of Cincinnati Graduate School Dean’s Fellowship When S. Wang was a graduate student. The authors acknowledge the United States Geological Survey (USGS) for the Declassified Intelligence Satellite Photography and Landsat images, the Alaska Satellite Facility for the ALOS PALSAR images, the European Space Agency for the ERS-1/2 and Envisat SAR images, the Byrd Polar and Climate Research Center at Ohio State University for the orthorectified Radarsat-1 SAR images and other RAMP data products, the National Snow and Ice Data Center for the Antarctic DEM data and the MEASUREs phase-based Antarctica ice velocity data, and the Jet Propulsion Laboratory and University of California at Irvine for the Ice-sheet and Sea-level System Model (ISSM).

There are no restrictions to access the data used for this study. The DISP imagery (<https://doi.org/10.5066/F78P5XZM>), Landsat-4/5 TM (<https://doi.org/10.5066/F7N015TQ>), Landsat-7 ETM+ (<https://doi.org/10.5066/F7WH2P8G>), and Landsat-8 OLI (<https://doi.org/10.5066/F71835S6>) images were downloaded from the USGS EarthExplorer data portal (<https://earthexplorer.usgs.gov/>), courtesy of the U.S. Geological Survey. The ALOS PALSAR images (© JAXA/METI ALOS PALSAR L1.5 2006-2010. Accessed through ASF DAAC 1 February 2014) were downloaded from the Alaska Satellite Facility data portal (<https://asf.alaska.edu/>). The Radarsat Antarctic Mapping Project (RAMP) data (<https://doi.org/10.5067/HHK2QT3LQMEL>) are available at <https://asf.alaska.edu/data-sets/derived-data-sets/ramp/ramp-get-ramp-data/>. ERS-1/2 SAR images were accessed from [https://earth.esa.int/eogateway/catalog/ers-1-2-sar-im-10-sar\\_im\\_\\_0p-](https://earth.esa.int/eogateway/catalog/ers-1-2-sar-im-10-sar_im__0p-), and Envisat ASAR images were accessed from [https://earth.esa.int/eogateway/catalog/envisat-asar-im-precision-11-asa\\_imp\\_1p-](https://earth.esa.int/eogateway/catalog/envisat-asar-im-precision-11-asa_imp_1p-), courtesy of European Space Agency. The DEM data were accessed from the National Snow and Ice Data Center (<https://nsidc.org/data/nsidc-0082> and <https://nsidc.org/data/NSIDC-0422/versions/1>) (Liu et

al., 2001; Bamber et al., 2009). The MEASUREs phase-based Antarctica ice velocity data are available at <https://nsidc.org/data/NSIDC-0754/versions/1> (Mouginot et al., 2019b). The Ice-sheet and Sea-level System Model (ISSM) is open source and publicly available at <https://issm.jpl.nasa.gov/> (Larour et al., 2012).

## References

- Adusumilli, S., Fricker, H. A., Siegfried, M. R., Padman, L., Paolo, F. S., & Ligtenberg, S. R. M. (2018). Variable Basal Melt Rates of Antarctic Peninsula Ice Shelves, 1994-2016. *Geophysical Research Letters*, *45* (9), 4086–4095. <https://doi.org/10.1002/2017gl076652>
- Adusumilli, S., Fricker, H. A., Medley, B., Padman, L., & Siegfried, M. R. (2020). Interannual variations in meltwater input to the Southern Ocean from Antarctic ice shelves. *Nature Geoscience*, *13* (9), 616–620. <https://doi.org/10.1038/s41561-020-0616-z>
- Alley, K. E., Scambos, T. A., Anderson, R. S., Rajaram, H., Pope, A., & Haran, T. M. (2018). Continent-wide estimates of Antarctic strain rates from Landsat 8-derived velocity grids. *Journal of Glaciology*, *64* (244), 321–332. <https://doi.org/10.1017/jog.2018.23>
- Alley, K. E., Scambos, T. A., Alley, R. B., & Holschuh, N. (2019). Troughs developed in ice-stream shear margins precondition ice shelves for ocean-driven breakup. *Science Advances*, *5* (10), eaax2215.
- Bamber, J. L., Gomez-Dans, J. L., & Griggs, J. A. (2009). Antarctic 1 km Digital Elevation Model (DEM) from Combined ERS-1 Radar and ICESat Laser Satellite Altimetry, Version 1. [Antarctic Peninsula]. Boulder, Colorado USA. NASA National Snow and Ice Data Center Distributed Active Archive Center. doi: <https://doi.org/10.5067/H0FQ1KL9NEKM>. [Date Accessed: 2019-01-01].
- Banwell, A. F., MacAyeal, D. R., & Sergienko, O. V. (2013). Breakup of the Larsen B Ice Shelf triggered by chain reaction drainage of supraglacial lakes. *Geophysical Research Letters*, *40* (22), 2013GL057694.
- Bell, R. E., Chu, W., Kingslake, J., Das, I., Tedesco, M., Tinto, K. J., et al. (2017). Antarctic ice shelf potentially stabilized by export of meltwater in surface river. *Nature*, *544* (7650), 344–348.
- Benn, D. I., Warren, C. R., & Mottram, R. H. (2007). Calving processes and the dynamics of calving glaciers. *Earth-Science Reviews*, *82* (3), 143–179.
- Bevan, S., Luckman, A., Hendon, H., & Wang, G. (2020). The 2020 Larsen C Ice Shelf surface melt is a 40-year record high. *The Cryosphere*, *14* (10), 3551–3564.
- Borstad, C., McGrath, D., & Pope, A. (2017). Fracture propagation and stability of ice shelves governed by ice shelf heterogeneity. *Geophysical Research Letters*, *44* (9), 4186–4194.
- Borstad, C. P., Khazendar, A., Larour, E., Morlighem, M., Rignot, E., Schodlok, M. P., & Seroussi, H. (2012). A damage mechanics assessment of the Larsen B ice shelf prior to collapse: Toward a physically-based calving law. *Geophysical Research Letters*, *39* (18), L18502.
- Borstad, C. P., Rignot, E., Mouginot, J., & Schodlok, M. P. (2013). Creep deformation and buttressing capacity of damaged ice shelves: theory and application to Larsen C ice shelf. *The Cryosphere*, *7* (6), 1931–1947.
- van den Broeke, M. (2005). Strong surface melting preceded collapse of Antarctic Peninsula ice shelf. *Geophysical Research Letters*, *32* (12), L12815.
- Colgan, W., Rajaram, H., Abdalati, W., McCutchan, C., Mottram, R., Moussavi, M. S., & Grigsby, S. (2016). Glacier crevasses: Observations, models, and mass balance implications. *Reviews of Geophysics*, *54* (1), 119–161.
- Cook, A. J., Fox, A. J., Vaughan, D. G., & Ferrigno, J. G. (2005). Retreating glacier fronts on the Antarctic Peninsula over the past half-century. *Science*, *308* (5721), 541–544.
- Cuffey, K. M., & Paterson, W. S. B. (2010). *The Physics of Glaciers*. Academic Press.

- DeConto, R. M., Pollard, D., Alley, R. B., Velicogna, I., Gasson, E., Gomez, N., et al. (2021). The Paris Climate Agreement and future sea-level rise from Antarctica. *Nature* , *593* (7857), 83–89.
- Depoorter, M. A., Bamber, J. L., Griggs, J. A., Lenaerts, J. T. M., Ligtenberg, S. R. M., van den Broeke, M. R., & Moholdt, G. (2013). Calving fluxes and basal melt rates of Antarctic ice shelves. *Nature* , *502* (7469), 89–92.
- Doake, C. S. M., & Vaughan, D. G. (1991). Rapid disintegration of the Wordie Ice Shelf in response to atmospheric warming. *Nature* , *350* (6316), 328–330.
- Doake, C. S. M., Corr, H. F. J., Rott, H., Skvarca, P., & Young, N. W. (1998). Breakup and conditions for stability of the northern Larsen Ice Shelf, Antarctica. *Nature* , *391* (6669), 778–780.
- Dow, C. F., Lee, W. S., Greenbaum, J. S., Greene, C. A., Blankenship, D. D., Poinar, K., et al. (2018). Basal channels drive active surface hydrology and transverse ice shelf fracture. *Science Advances* , *4* (6), eaao7212.
- Dupont, T. K., & Alley, R. B. (2005). Assessment of the importance of ice-shelf buttressing to ice-sheet flow. *Geophysical Research Letters* , *32* (4). <https://doi.org/10.1029/2004GL022024>
- Elvidge, A. D., Renfrew, I. A., King, J. C., Orr, A., Lachlan-Cope, T. A., Weeks, M., & Gray, S. L. (2015). Foehn jets over the Larsen C Ice Shelf, Antarctica. *Quarterly Journal of the Royal Meteorological Society* , *141* (688), 698–713.
- Elvidge, A. D., Kuipers Munneke, P., King, J. C., Renfrew, I. A., & Gilbert, E. (2020). Atmospheric drivers of melt on Larsen C ice shelf: Surface energy budget regimes and the impact of foehn. *Journal of Geophysical Research* , *125* (17). <https://doi.org/10.1029/2020jd032463>
- Favier, L., & Pattyn, F. (2015). Antarctic ice rise formation, evolution, and stability. *Geophysical Research Letters* , *42* (11), 2015GL064195.
- Ferrigno, J. G., & Gould, W. G. (1987). Substantial changes in the coastline of Antarctica revealed by satellite imagery. *Polar Record* , *23* (146), 577–583. <https://doi.org/10.1017/s003224740000807x>
- Fürst, J. J., Durand, G., Gillet-Chaulet, F., Tavard, L., Rankl, M., Braun, M., & Gagliardini, O. (2016). The safety band of Antarctic ice shelves. *Nature Climate Change* , *6* (5), 479–482.
- Gagliardini, O., Durand, G., Zwinger, T., Hindmarsh, R. C. A., & Le Meur, E. (2010). Coupling of ice-shelf melting and buttressing is a key process in ice-sheets dynamics. *Geophysical Research Letters* , *37* (14). <https://doi.org/10.1029/2010GL043334>
- Glasser, N. F., Kulesa, B., Luckman, A., Jansen, D., King, E. C., Sammonds, P. R., et al. (2009). Surface structure and stability of the Larsen C ice shelf, Antarctic Peninsula. *Journal of Glaciology* , *55* (191), 400–410.
- Gudmundsson, G. H. (2013). Ice-shelf buttressing and the stability of marine ice sheets. *The Cryosphere* , *7* (2), 647–655.
- Heid, T., & Kääh, A. (2012). Evaluation of existing image matching methods for deriving glacier surface displacements globally from optical satellite imagery. *Remote Sensing of Environment* , *118* , 339–355. <https://doi.org/10.1016/j.rse.2011.11.024>
- Hogg, A. E., & Hilmar Gudmundsson, G. (2017). Impacts of the Larsen-C Ice Shelf calving event. *Nature Climate Change* , *7* (8), 540–542. <https://doi.org/10.1038/nclimate3359>
- Holland, P. R., Corr, H. F. J., Vaughan, D. G., Jenkins, A., & Skvarca, P. (2009). Marine ice in Larsen Ice Shelf. *Geophysical Research Letters* , *36* (11), L11604.
- Holland, P. R., Brisbourne, A., Corr, H. F. J., McGrath, D., Purdon, K., Paden, J., et al. (2015). Oceanic and atmospheric forcing of Larsen C Ice-Shelf thinning. *The Cryosphere* , *9* (3), 1005–1024.

- Howat, I. M., Porter, C., Smith, B. E., Noh, M.-J., & Morin, P. (2019). The Reference Elevation Model of Antarctica. *The Cryosphere* , 13 (2), 665–674. <https://doi.org/10.5194/tc-13-665-2019>
- Hulbe, C. L., LeDoux, C., & Cruikshank, K. (2010). Propagation of long fractures in the Ronne Ice Shelf, Antarctica, investigated using a numerical model of fracture propagation. *Journal of Glaciology* ,56 (197), 459–472.
- Jansen, D., Kulesa, B., Sammonds, P. R., Luckman, A., King, E. C., & Glasser, N. F. (2010). Present stability of the Larsen C ice shelf, Antarctic Peninsula. *Journal of Glaciology* , 56 (198), 593–600.
- Jansen, D., Luckman, A., Kulesa, B., Holland, P. R., & King, E. C. (2013). Marine ice formation in a suture zone on the Larsen C Ice Shelf and its influence on ice shelf dynamics. *Journal of Geophysical Research: Earth Surface* , 118 (3), 1628–1640.
- Jansen, D., Luckman, A. J., Cook, A., Bevan, S., Kulesa, B., Hubbard, B., & Holland, P. R. (2015). Brief Communication: Newly developing rift in Larsen C Ice Shelf presents significant risk to stability. *The Cryosphere* , 9 (3), 1223–1227.
- Jezeq, K. C. (2003). Observing the Antarctic Ice Sheet Using the RADARSAT-1 Synthetic Aperture Radar. *Polar Geography* ,27 (3), 197–209.
- Jezeq, K. C., Sohn, H. G., & Noltimier, K. F. (1998). The RADARSAT Antarctic Mapping Project. *IGARSS '98. Sensing and Managing the Environment. 1998 IEEE International Geoscience and Remote Sensing Symposium Proceedings. (Cat. No.98CH36174)* . <https://doi.org/10.1109/igarss.1998.702246>
- Joughin, I., Howat, I. M., Fahnestock, M., Smith, B., Krabill, W., Alley, R. B., et al. (2008). Continued evolution of Jakobshavn Isbrae following its rapid speedup. *Journal of Geophysical Research* ,113 (F4). <https://doi.org/10.1029/2008jf001023>
- King, J. C., Kirchgassner, A., Bevan, S., Elvidge, A. D., Kuipers Munneke, P., Luckman, A., et al. (2017). The Impact of Föhn Winds on Surface Energy Balance During the 2010–2011 Melt Season Over Larsen C Ice Shelf, Antarctica. *Journal of Geophysical Research, D: Atmospheres* , 122 (22), 2017JD026809.
- Krug, J., Weiss, J., Gagliardini, O., & Durand, G. (2014). Combining damage and fracture mechanics to model calving. *The Cryosphere* , 8 (6), 2101–2117. <https://doi.org/10.5194/tcd-8-1111-2014>
- Kulesa, B., Jansen, D., Luckman, A. J., King, E. C., & Sammonds, P. R. (2014). Marine ice regulates the future stability of a large Antarctic ice shelf. *Nature Communications* , 5 , 3707.
- Kulesa, B., Booth, A. D., O’Leary, M., McGrath, D., King, E. C., Luckman, A. J., et al. (2019). Seawater softening of suture zones inhibits fracture propagation in Antarctic ice shelves. *Nature Communications* , 10 (1), 5491.
- Lai, C.-Y., Kingslake, J., Wearing, M. G., Chen, P.-H. C., Gentine, P., Li, H., et al. (2020). Vulnerability of Antarctica’s ice shelves to meltwater-driven fracture. *Nature* , 584 (7822), 574–578. <https://doi.org/10.1038/s41586-020-2627-8>
- Larour, E., Seroussi, H., Morlighem, M., & Rignot, E. (2012). Continental scale, high order, high spatial resolution, ice sheet modeling using the Ice Sheet System Model (ISSM). *Journal of Geophysical Research: Earth Surface* , 117 (F1). <https://doi.org/10.1029/2011jf002140>
- Lhermitte, S., Sun, S., Shuman, C., Wouters, B., Pattyn, F., Wuite, J., et al. (2020). Damage accelerates ice shelf instability and mass loss in Amundsen Sea Embayment. *Proceedings of the National Academy of Sciences of the United States of America* , 117 (40), 24735–24741.
- Lipovsky, B. P. (2020). Ice shelf rift propagation: stability, three-dimensional effects, and the role of marginal weakening. *The Cryosphere* , 14 (5), 1673–1683. <https://doi.org/10.5194/tc-14-1673-2020>

- Liu, H., Jezek, K., Li, B., & Zhao, Z. (2001). Radarsat Antarctic Mapping Project digital elevation model version 2. *Radarsat Antarctic Mapping Project Digital Elevation Model Version 2*, Boulder, Colorado USA: National Snow and Ice Data Center. *Digital Media*.
- Liu, H., Wang, L., Tang, S.-J., & Jezek, K. C. (2012). Robust multi-scale image matching for deriving ice surface velocity field from sequential satellite images. *International Journal of Remote Sensing* , 33 (6), 1799–1822.
- Liu, Y., Moore, J. C., Cheng, X., Gladstone, R. M., Bassis, J. N., Liu, H., et al. (2015). Ocean-driven thinning enhances iceberg calving and retreat of Antarctic ice shelves. *Proceedings of the National Academy of Sciences of the United States of America* , 112 (11), 3263–3268.
- Luckman, A., Elvidge, A., Jansen, D., Kulesa, B., Munneke, P. K., King, J., & Barrand, N. E. (2014). Surface melt and ponding on Larsen C Ice Shelf and the impact of föhn winds. *Antarctic Science / Blackwell Scientific Publications* , 26 (6), 625–635.
- MacAyeal, D. R. (1989). Large-scale ice flow over a viscous basal sediment: Theory and application to ice stream B, Antarctica. *Journal of Geophysical Research* , 94 (B4), 4071–4087.
- MacAyeal, D. R., Scambos, T. A., Hulbe, C. L., & Fahnestock, M. A. (2003). Catastrophic ice-shelf break-up by an ice-shelf-fragment-capsize mechanism. *Journal of Glaciology* , 49 (164), 22–36.
- Matsuoka, K., Hindmarsh, R. C. A., Moholdt, G., Bentley, M. J., Pritchard, H. D., Brown, J., et al. (2015). Antarctic ice rises and rumples: Their properties and significance for ice-sheet dynamics and evolution. *Earth-Science Reviews* , 150 , 724–745.
- McGrath, D., Steffen, K., Holland, P. R., Scambos, T., Rajaram, H., Abdalati, W., & Rignot, E. (2014). The structure and effect of suture zones in the Larsen C Ice Shelf, Antarctica. *Journal of Geophysical Research: Earth Surface* , 119 (3), 588–602.
- Morland, L. W. (1987). Unconfined Ice-Shelf Flow. In *Dynamics of the West Antarctic Ice Sheet* (pp. 99–116). Springer Netherlands.
- Morlighem, M., Seroussi, H., Larour, É., Schlegel, N., Borstad, C., de Fleurian, B., et al. (2015). Ice sheet system model 2015 (4.9) user guide. Retrieved June 30, 2021, from <http://www.ccpo.odu.edu/~klinck/Reprints/PDF/ISSMguide2015.pdf>
- Morris, E. M., & Vaughan, D. G. (2003). Spatial and Temporal Variation of Surface Temperature on the Antarctic Peninsula And The Limit of Viability of Ice Shelves. In *Antarctic Peninsula Climate Variability: Historical and Paleoenvironmental Perspectives* (pp. 61–68). American Geophysical Union.
- Mouginot, J., Rignot, E., & Scheuchl, B. (2019a). Continent-wide, interferometric SAR phase, mapping of antarctic ice velocity. *Geophysical Research Letters* , 46 (16), 9710–9718.
- Mouginot, J., Rignot, E., & Scheuchl, B. (2019b). *MEaSURES Phase-Based Antarctica Ice Velocity Map, Version 1* . [Antarctic Peninsula]. Boulder, Colorado USA. NASA National Snow and Ice Data Center Distributed Active Archive Center. doi: <https://doi.org/10.5067/PZ3NJ5RXHRH10>. [Access date: 2020-10-01].
- Noble, T. L., Rohling, E. J., Aitken, A. R. A., Bostock, H. C., Chase, Z., Gomez, N., et al. (2020). The sensitivity of the antarctic ice sheet to a changing climate: Past, present, and future. *Reviews of Geophysics*, 58 (4). <https://doi.org/10.1029/2019rg000663>
- Paolo, F. S., Fricker, H. A., & Padman, L. (2015). Ice sheets. Volume loss from Antarctic ice shelves is accelerating. *Science* , 348 (6232), 327–331.
- Pattyn, F., & Morlighem, M. (2020). The uncertain future of the Antarctic Ice Sheet. *Science* , 367 (6484), 1331–1335.

- Pritchard, H. D., Ligtenberg, S. R. M., Fricker, H. A., Vaughan, D. G., van den Broeke, M. R., & Padman, L. (2012). Antarctic ice-sheet loss driven by basal melting of ice shelves. *Nature* , 484 (7395), 502–505.
- Reese, R., Gudmundsson, G. H., Levermann, A., & Winkelmann, R. (2017). The far reach of ice-shelf thinning in Antarctica. *Nature Climate Change* , 8 (1), 53–57.
- Rignot, E., Casassa, G., Gogineni, P., Krabill, W., Rivera, A., & Thomas, R. (2004). Accelerated ice discharge from the Antarctic Peninsula following the collapse of Larsen B ice shelf. *Geophysical Research Letters* , 31 (18), L18401.
- Rignot, E., Jacobs, S., Mouginot, J., & Scheuchl, B. (2013). Ice-shelf melting around Antarctica. *Science* , 341 (6143), 266–270.
- Robel, A. A., & Banwell, A. F. (2019). A speed limit on ice shelf collapse through hydrofracture. *Geophysical Research Letters* , 46 (21), 12092–12100.
- Rott, H., Skvarca, P., & Nagler, T. (1996). Rapid collapse of northern Larsen ice shelf, Antarctica. *Science* , 271 (5250), 788.
- Scambos, T., Hulbe, C., & Fahnestock, M. (2003). Climate-induced ice shelf disintegration in the Antarctic peninsula. *Antarctic Peninsula Climate Variability: Historical and Paleoenvironmental Perspectives* , 79–92.
- Scambos, T., Fricker, H. A., Liu, C.-C., Bohlander, J., Fastook, J., Sargent, A., et al. (2009). Ice shelf disintegration by plate bending and hydro-fracture: Satellite observations and model results of the 2008 Wilkins ice shelf break-ups. *Earth and Planetary Science Letters* , 280 (1), 51–60.
- Scambos, T. A., Dutkiewicz, M. J., Wilson, J. C., & Bindshadler, R. A. (1992). Application of image cross-correlation to the measurement of glacier velocity using satellite image data. *Remote Sensing of Environment* , 42 (3), 177–186.
- Scambos, T. A., Hulbe, C., Fahnestock, M., & Bohlander, J. (2000). The link between climate warming and break-up of ice shelves in the Antarctic Peninsula. *Journal of Glaciology* , 46 (154), 516–530.
- Scambos, T. A., Bohlander, J. A., Shuman, C. A., & Skvarca, P. (2004). Glacier acceleration and thinning after ice shelf collapse in the Larsen B embayment, Antarctica. *Geophysical Research Letters* , 31 (18), L18402.
- Shepherd, A., Wingham, D., Payne, T., & Skvarca, P. (2003). Larsen ice shelf has progressively thinned. *Science* , 302 (5646), 856–859.
- Skvarca, P. (1994). Changes and surface features of the Larsen Ice Shelf, Antarctica, derived from Landsat and Kosmos mosaics. *Annals of Glaciology* , 20 , 6-12. <https://doi.org/10.3189/1994aog20-1-6-12>
- Small, D., Schubert, A., Rosich, B., Meier, E., Lacoste, H., & Ouwehand, L. (2007). Geometric and radiometric correction of ESA SAR products. In H. Lacoste & L. Ouwehand (Eds.) (p. online). Presented at the Envisat Symposium 2007, Montreux (CH): European Space Agency \* Communication Production Office.
- Thomas, R. H. (1979). Ice Shelves: A Review. *Journal of Glaciology* , 24 (90), 273–286.
- Vaughan, D. G., & Doake, C. S. M. (1996). Recent atmospheric warming and retreat of ice shelves on the Antarctic Peninsula. *Nature* , 379 (6563), 328–331.
- Vaughan, D. G., Marshall, G. J., Connolley, W. M., Parkinson, C., Mulvaney, R., Hodgson, D. A., et al. (2003). Recent Rapid Regional Climate Warming on the Antarctic Peninsula. *Climatic Change* , 60 (3), 243–274.
- Vieli, A., Payne, A. J., Shepherd, A., & Du, Z. (2007). Causes of pre-collapse changes of the Larsen B ice shelf: Numerical modelling and assimilation of satellite observations. *Earth and Planetary Science Letters* , 259 (3), 297–306.

Wang, S., Liu, H., Yu, B., Zhou, G., & Cheng, X. (2016). Revealing the early ice flow patterns with historical Declassified Intelligence Satellite Photographs back to 1960s. *Geophysical Research Letters* , 43 (11), 2016GL068990.

Wang, S., Alexander, P., Wu, Q., Tedesco, M., & Shu, S. (2021). Characterization of ice shelf fracture features using ICESat-2 – A case study over the Amery Ice Shelf. *Remote Sensing of the Environment* , 255 , 112266.

Weis, M., Greve, R., & Hutter, K. (1999). Theory of shallow ice shelves. *Continuum Mechanics and Thermodynamics* , 11 (1), 15–50.

Shujie Wang<sup>1,2,3</sup>, Hongxing Liu<sup>4,5</sup>, Kenneth Jezek<sup>6</sup>, Richard B. Alley<sup>2,7</sup>, Lei Wang<sup>8</sup>, Patrick Alexander<sup>9</sup>, and Yan Huang<sup>5</sup>

<sup>1</sup>Department of Geography, Pennsylvania State University, University Park, PA 16802, USA.

<sup>2</sup>Earth and Environmental Systems Institute, Pennsylvania State University, University Park, PA 16802, USA.

<sup>3</sup>Institute for Computational and Data Sciences, Pennsylvania State University, University Park, PA 16802, USA.

<sup>4</sup>Department of Geography, University of Alabama, Tuscaloosa, AL 35487, USA.

<sup>5</sup>Key Laboratory of Geographic Information Science, Ministry of Education, East China Normal University, Shanghai 200241, China.

<sup>6</sup>School of Earth Sciences, Ohio State University, Columbus, OH 43210, USA.

<sup>7</sup>Department of Geosciences, Pennsylvania State University, University Park, PA 16802, USA.

<sup>8</sup>Department of Geography & Anthropology, Louisiana State University, Baton Rouge, LA 70803, USA.

<sup>9</sup>Lamont-Doherty Earth Observatory, Columbia University, Palisades, NY 10964, USA.

Corresponding author: Shujie Wang (skw5660@psu.edu)

Key Points:

- Multidecadal satellite images and ice shelf modeling experiments were used to examine dynamic changes of Larsen C during 1963–2020
- Rift development near ice rises is a primary control on ice shelf retreat and flow acceleration before the compressive arch is reached
- Capturing the time-varying effects of rifts on ice rigidity is needed to make realistic simulations of future ice shelf change

Abstract

Rapid retreat of the Larsen A and B ice shelves has provided important clues about the ice shelf destabilization processes. The Larsen C Ice Shelf, the largest remaining ice shelf on the Antarctic Peninsula, may also be vulnerable to future collapse in a warming climate. Here, we utilize multi-source satellite images collected over 1963–2020 to derive multidecadal time series of ice front, flow velocities, and critical rift features over Larsen C, with the aim of understanding the controls on its retreat. We complement these observations with modeling experiments using the Ice-sheet and Sea-level System Model to examine how front geometry conditions and mechanical weakening due to rifts affect ice shelf dynamics. Over the past six decades, Larsen C lost over 20% of its area, dominated by rift-induced tabular iceberg calving. The Bawden Ice Rise and Gipps

Ice Rise are critical areas for rift formation, through their impact on the longitudinal deviatoric stress field. Mechanical weakening around Gipps Ice Rise is found to be a primary control on localized flow acceleration, leading to the propagation of two rifts that caused a major calving event in 2017. Capturing the time-varying effects of rifts on ice rigidity in ice shelf models is essential for making realistic predictions of ice shelf flow dynamics and instability. In the context of the Larsen A and Larsen B collapses, we infer a chronology of destabilization processes for embayment-confined ice shelves, which provides a useful framework for understanding the historical and future destabilization of Antarctic ice shelves.

### **Plain Language Summary**

The Antarctic Ice Sheet is the largest source of uncertainty in projecting future sea-level rise. This is due to our limited understanding of drivers and mechanisms triggering tipping points in ice-sheet instability, and knowledge gaps regarding the retreat and disintegration of ice shelves. Understanding processes leading to ice shelf destabilization is critical to improving estimates of future Antarctic mass loss because of their important role in stabilizing ice flow. We studied Larsen C Ice Shelf changes using satellite data collected over 1963–2020, and conducted modeling experiments to elucidate the observed linkages between front retreat, flow acceleration, and rifts. We find the development of rifts near ice rises to be the primary control on Larsen C front calving and flow acceleration in the past six decades. Rifts can affect each other by causing structural weakening and modifying stress fields. To predict future dynamical changes, it is necessary to account for this feedback and capture how ice rigidity changes over time in response to rift growth. If Larsen C retreats such that the compressive arch ceases to exist, it will resemble the pre-collapsed Larsen B ice shelf, producing widespread flow accelerations in response to the backstress loss from ice rises.

### **1 Introduction**

Ice shelves, as floating extensions of the grounded ice sheet, fringe ~75% of Antarctica’s coastline (Rignot et al., 2013). Ice shelves gain mass through ice flux from inland glaciers, local snow accumulation, and basal marine ice accretion, while they lose mass primarily via basal melting and iceberg calving (e.g., Depoorter et al., 2013; Liu et al., 2015), together with minor runoff of surface meltwater (Bell et al., 2017). Although the direct effect of ice shelf mass loss on sea-level rise is negligible, ice shelves provide an important buttressing force to stabilize the grounded ice sheet and regulate the contribution from inland glaciers to global sea level (Dupont & Alley, 2005; Gagliardini et al., 2010; Gudmundsson, 2013; Pritchard et al., 2012; Reese et al., 2017; Thomas, 1979). Understanding the processes driving ice shelf retreat is therefore essential to generating realistic projections of future Antarctic ice sheet mass loss in a warming climate (DeConto et al., 2021; Noble et al., 2020; Pattyn & Morlighem, 2020).

Satellite data have indicated increasing trends in thinning and retreat of Antarc-

tic ice shelves (e.g., Depoorter et al., 2013; Paolo et al., 2015), revealing the vulnerability of ice shelves to atmospheric warming and oceanic forcing (Holland et al., 2015; Liu et al., 2015; Vaughan & Doake, 1996). As a region sensitive to climate warming, the Antarctic Peninsula has undergone pronounced regional warming (Vaughan et al., 2003), along with rapid retreat of ice shelves and glaciers on both the west and east coasts (Cook et al., 2005; Doake & Vaughan, 1991; Rott et al., 1996; Scambos et al., 2009; Scambos et al., 2004). Successive retreat has occurred on the Larsen Ice Shelf along the east coast. The Larsen Ice Shelf was formerly composed of Larsen A, B, C, and D, four sections from north to south (Figure 1). Larsen A disintegrated in 1995, with an areal loss of  $\sim 1600 \text{ km}^2$  (Rott et al., 1996). Larsen B collapsed in February–March 2002, with an areal loss of  $\sim 3250 \text{ km}^2$  (Scambos et al., 2004). The rapid disintegrations of Larsen A and Larsen B triggered immediate flow accelerations of upstream glaciers (Rignot et al., 2004; Scambos et al., 2004), which highlights the importance of studying how an ice shelf evolves to an unstable condition and how ice shelf retreat affects upstream flow dynamics. This has also led to an increasing concern as to whether Larsen C will disintegrate in the future (e.g., Borstad et al., 2017; Glasser et al., 2009; Hogg & Gudmundsson, 2017; Jansen et al., 2010, 2015; Kulessa et al., 2014), especially after a giant iceberg (A68,  $\sim 5800 \text{ km}^2$ ) broke off from Larsen C in July 2017.

The disintegrations of Larsen A and Larsen B were preceded by warm air temperature and intense surface melt (Banwell et al., 2013; Scambos et al., 2003; Scambos et al., 2000). Meltwater-induced hydrofracturing has been postulated to be the dominant mechanism in the ice shelf collapse (van den Broeke, 2005; MacAyeal et al., 2003; Robel & Banwell, 2019), likely preconditioned by increased basal melting (Shepherd et al., 2003; Vieli et al., 2007). To predict the future stability of Larsen C, recent research has focused on surface melt and associated atmospheric drivers (Bevan et al., 2020; Luckman et al., 2014), and parallel efforts have focused on ocean-driven basal processes (Holland et al., 2015; Jansen et al., 2013; McGrath et al., 2014), such as basal melting and the stabilizing role of suture zones. Despite the importance of atmospheric and oceanic forcing, the stability of an ice shelf is also controlled by its stress field (Doake et al., 1998; Fürst et al., 2016; Kulessa et al., 2014; Lhermitte et al., 2020). The stress field, either compressive or tensile, is closely related to fracture opening. The spatial distribution and temporal evolution of fractures determine the ice shelf resilience, and enhanced fracturing along shear margins has been suggested to be critical for ice shelf stability and flow dynamics (Lhermitte et al., 2020; Joughin et al. 2008). Larsen A and Larsen B were already in an unstable stress state before their collapse as the front retreat had passed a “compressive arch” (Doake et al., 1998). Investigating the dynamic changes of ice shelves over the long term is important to understanding the destabilization processes. Multidecadal satellite observations on the retreat of Larsen C provide an excellent opportunity to study the long-term dynamic behavior of ice shelves and associated rifting and calving processes. Understanding these processes is also the key to predicting the future changes of other embayment-confined ice

shelves, such as the Ross Ice Shelf and Filchner–Ronne Ice Shelf.

Here, we use multi-source satellite images spanning six decades and ice shelf modeling experiments to conduct a comprehensive analysis of the changes of ice shelf front, flow velocities, and stress fields over Larsen C. The earliest satellite imagery acquired in the 1960s allows us to extend the flow velocity data back to the 1960s–1980s. We analyze in detail the development of two rifts that led to the 2017 calving event, and reveal the close linkages between rift propagation, flow acceleration, and front retreat. We further carry out ice shelf modeling experiments to examine how ice shelf flow velocities and stress fields vary in response to the front geometry change due to ice shelf retreat and the mechanical weakening due to rift development.

## 2 Study area

Larsen C is confined by Jason Peninsula in the north and Kenyon Peninsula and Gipps Ice Rise in the south (Figure 1). Because of the barrier effect of the high mountain ridge on westerly winds, the east side of the Antarctic Peninsula is generally colder than the west side (King et al., 2017; Morris & Vaughan, 2003). However, strong downslope foehn winds occasionally bring warm and dry air masses over the northern Larsen C during the austral summer, causing intense surface melt in the northwest near the Cabinet Inlet (Elvidge et al., 2015; King et al., 2017). The structure of Larsen C (Figure 1) consists of fast flow units draining from the twelve inlets, and suture zones originating from the Churchill Peninsula, Cole Peninsula, Marmelon Point, Francis Island, Tonkin Island, and Joerg Peninsula (Borstad et al., 2017; Glasser et al., 2009). Suture zones connect those fast flow units and have been believed to play a significant role in stabilizing the ice shelf (Kulesa et al., 2014; McGrath et al., 2014). Two pinning points, the Bawden Ice Rise and Gipps Ice Rise, anchor the northern and southern ice front, respectively. The ice thickness varies from ~1000 m near the grounding line to ~200 m near the ice front.

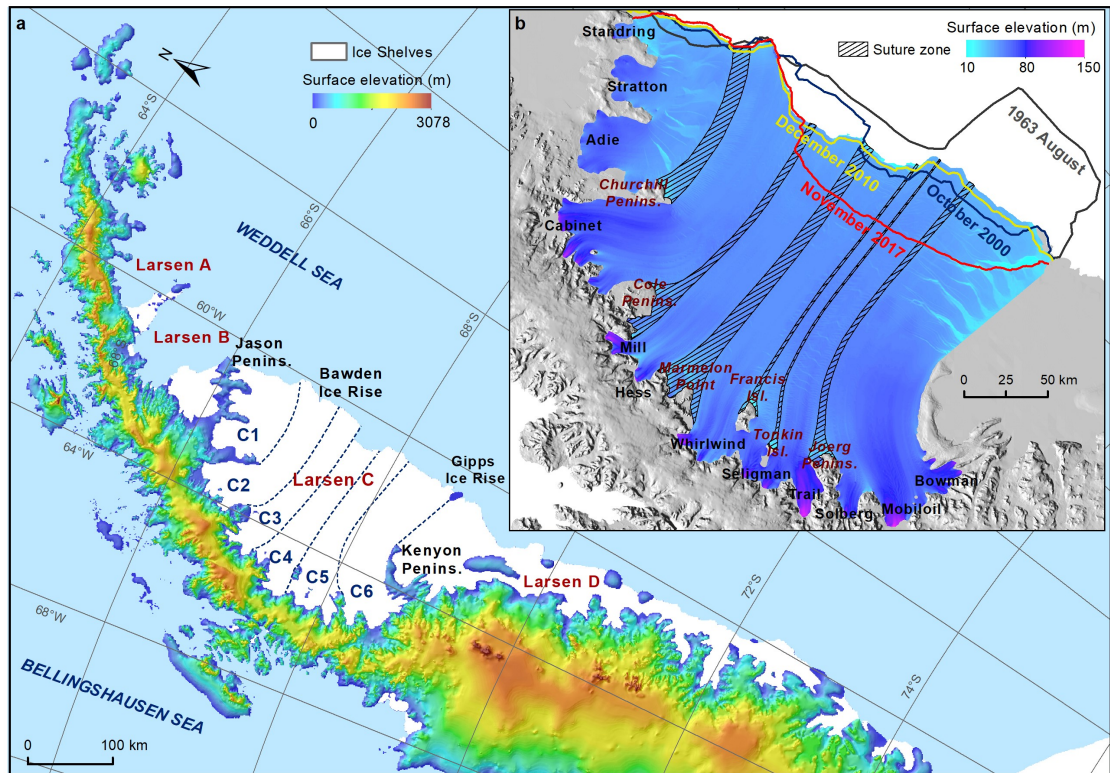


**Figure 1.** Study area. **a.** Larsen Ice Shelf (A, B, C, and D) from north to south. The white area is the ice shelf extent in 2015. The color-coded area shows the surface topography of the grounded region. We divided Larsen C into six flow units (C1, C2, C3, C4, C5, and C6). **b.** The ice front locations in 1963, 2000, 2010, and 2017 with the ice shelf surface elevations from REMA DEM (Howat et al., 2019), twelve flow inlets, and suture zones flowing from peninsulas and islands.

### 3 Data and Methods

#### 3.1 Mapping ice front, rifts, and flow velocities

We used multi-source satellite images acquired between 1963 and 2020 to map the ice front, identify rifts, and derive flow velocities in different time periods. The images include declassified intelligence satellite photographs (DISP) acquired by the ARGON mission, optical images acquired by the Landsat-4/5 TM, Landsat-7 ETM+, and Landsat-8 OLI sensors, and synthetic aperture radar (SAR) images acquired by the ERS-1, ERS-2, Radarsat-1, Envisat, and ALOS satellites. We performed image orthorectification, image co-registration, noise reduction, and image enhancement on the above set of images (Text S1).

We mapped the ice front locations of Larsen C for the period 1963 to 2020

(Figure S1) and delineated two rifts in the vicinity of Gipps Ice Rise that were closely related to the 2017 calving event. We derived flow velocities over the ice shelf for multiple periods using an image-matching-based feature tracking method (e.g., Heid & Kääh, 2012; Liu et al., 2012; Scambos et al., 1992). The feature tracking method tracks the spatial displacements of moving and identical surface features from two sequential images acquired at different times. The derived flow velocity represents the average velocity between the acquisition dates of sequential images. The image-matching algorithm automatically searches for matching points between two images by maximizing the cross-correlation coefficient between conjugate areas in the two images. The cross-correlation-based method can achieve an accuracy of better than 0.5 pixel (Scambos et al., 1992). For our study, the image space was examined every 300 m to search for matching points, with a matching window of 64x64 pixels. Automated directional and local statistical filters (Liu et al., 2012) plus human inspection were employed to remove erroneous matches and verify the matching results. The accuracy of the derived velocity fields is determined by the image co-registration accuracy, image matching accuracy, and time separation of sequential images, which was estimated to be 3.7~25 m/year, depending on the image pairs used (Table S1).

### 3.2 Ice shelf modeling experiments

We used the Ice-sheet and Sea-level System Model (ISSM) (Larour et al., 2012) to conduct the ice shelf modeling experiments. We used the shallow shelf approximation (SSA) model (MacAyeal 1989; Weis et al. 1999; Morland 1987) to examine how ice shelf flow velocities and stress fields vary with front retreat and rift development (Text S2). For the model configuration, we used the anisotropic mesh adaptation method to generate the numerical mesh net nodes. The boundary condition was specified as kinematic for the interior ice shelf and dynamic for the ice shelf front. The flow law exponent  $n$  was set to 3. The ice rigidity  $\bar{B}$  was initialized as  $1.5 \times 10^8 \text{ Pa s}^{1/3}$ . For the inversion of  $\bar{B}$ , we used the MIQN3 optimization algorithm in ISSM (Morlighem et al., 2015) by minimizing a cost function defined as the weighted sum of the difference between the modeled and observed flow velocity fields and the gradient of the optimized  $\bar{B}$  at each iteration. We further calculated the deviatoric stresses, including longitudinal deviatoric stresses and principal stresses (Text S1). We also calculated the backstress across the ice shelf. Backstress describes the stress transmitted upstream that opposes spreading of an ice shelf (Cuffey and Paterson, 2010), arising from side drag by lateral walls and slower flowing ice, and from basal resistance from grounded ice rises or ice rumples. These stress fields are tightly related to rift growth and ice shelf instability development.

## 4 Observations derived from satellite data

### 4.1 Retreat history of Larsen C during 1963–2020

During the period from August 1963 to March 2020 (Figure S1), the area of Larsen C decreased from 55,511 km<sup>2</sup> to 43,182 km<sup>2</sup>, a reduction of ~22%. In the six decades, Larsen C underwent two large retreat cycles, during 1976–1986,

and during 2004–2017. Each cycle began with northern retreat near the Bawden Ice Rise (C1–C3 units), followed by southern retreat near the Gipps Ice Rise (C4–C6 units). For both cycles, the time interval between the northern and southern retreat was approximately ten years. In the first cycle, the northern retreat occurred at the C2–C3 units in 1976 due to a collision between an iceberg and the ice shelf (Ferrigno & Gould, 1987); afterwards, two large icebergs calved off from the C4–C6 units in 1986 (Skvarca, 1994), causing a retreat of ~100 km in the south. The ice shelf slowly advanced between 1986 and 2004. In the second cycle, the northern front detached from the C2–C3 units in 2004/2005, with an area loss of ~1500 km<sup>2</sup>. The major retreat of the southern front happened on 12 July 2017, when a ~5800-km<sup>2</sup> tabular iceberg detached from the C3–C6 units.

#### 4.2 Rifting related to the 2017 calving event

The 2017 calving event resulted from the propagation of two rifts (labeled R1 and R2, Figure 2). Long and transverse fractures (Figure 2a) tend to form between Kenyon Peninsula and Gipps Ice Rise due to a stress condition change, where ice shelf flow becomes less constrained by the lateral shear margins after passing by Kenyon Peninsula. The majority of the fractures terminate near the Joerg suture zone (Figure 2a). Suture zones can inhibit fracture growth because of the material properties of marine ice underneath (Kulesa et al., 2014, 2019; McGrath et al., 2014). The rift R1, a transverse rift propagating perpendicular to the flow direction, developed from a preexisting fracture (L1 in Figure 2a) that is identifiable on the 1963 DISP imagery. The lateral extent of R1 changed little until 2008, when it began to propagate towards R2. By 2010, the southern rift tip of R1 had traveled ~14 km from its 2006 location (from A' to A, Figure 2c), to a point less than 1 km from R2. At the northern end, R1 developed a new rift trajectory from point B' to B (Figure 2c), and subsequently propagated to the north along this trajectory. R2 was an oblique rift that formed between Gipps Ice Rise and a transverse fracture (L2 in Figure 2a). R2 is not present on the 1963 DISP imagery. Its formation was very likely due to the front geometry change caused by the 1986 retreat. R2 widened over time, while its rift tips exhibited little change until 2013. Then, it began developing towards the south, and the rift tip almost reached Gipps Ice Rise (Figure 2e). Simultaneously, R1 penetrated through the Joerg suture zone and started rapid propagation to the north (Figure 2d). R1 cut through the C5 unit in 2014 and had propagated across the Tonkin suture zone by January 2016 (Figure 2d). By March 2017, the length of R1 dramatically increased by ~65 km, and its northern rift tip ('B') reached the Cole Peninsula suture zone (connecting the C2 and C3 units). R1 continued penetrating through the Cole Peninsula suture zone, but did not extend into the C2 unit. Instead, it was developing along the C2 unit boundary towards the ice front, resulting in the complete detachment of the downstream portion in July 2017.

The propagation of R1 appears to have had a strong association with the development of R2. The extension of R2 to Gipps Ice Rise was immediately followed by the rapid growth of R1 towards the north. This suggests that rifting can

promote the growth of another rift by weakening the lateral shear margins near an ice rise. Ice rises are locally grounded topographic highs in ice shelves. They often act as pinning points, buttress upstream ice flows and play an active role in ice shelf stability (Favier & Pattyn, 2015; Matsuoka et al., 2015). Weakening around ice rises could reduce their buttressing effect, leading to enhanced longitudinal stretching and creating favorable conditions for rift propagation. We further explore this hypothesis through modeling experiments in Section 5.

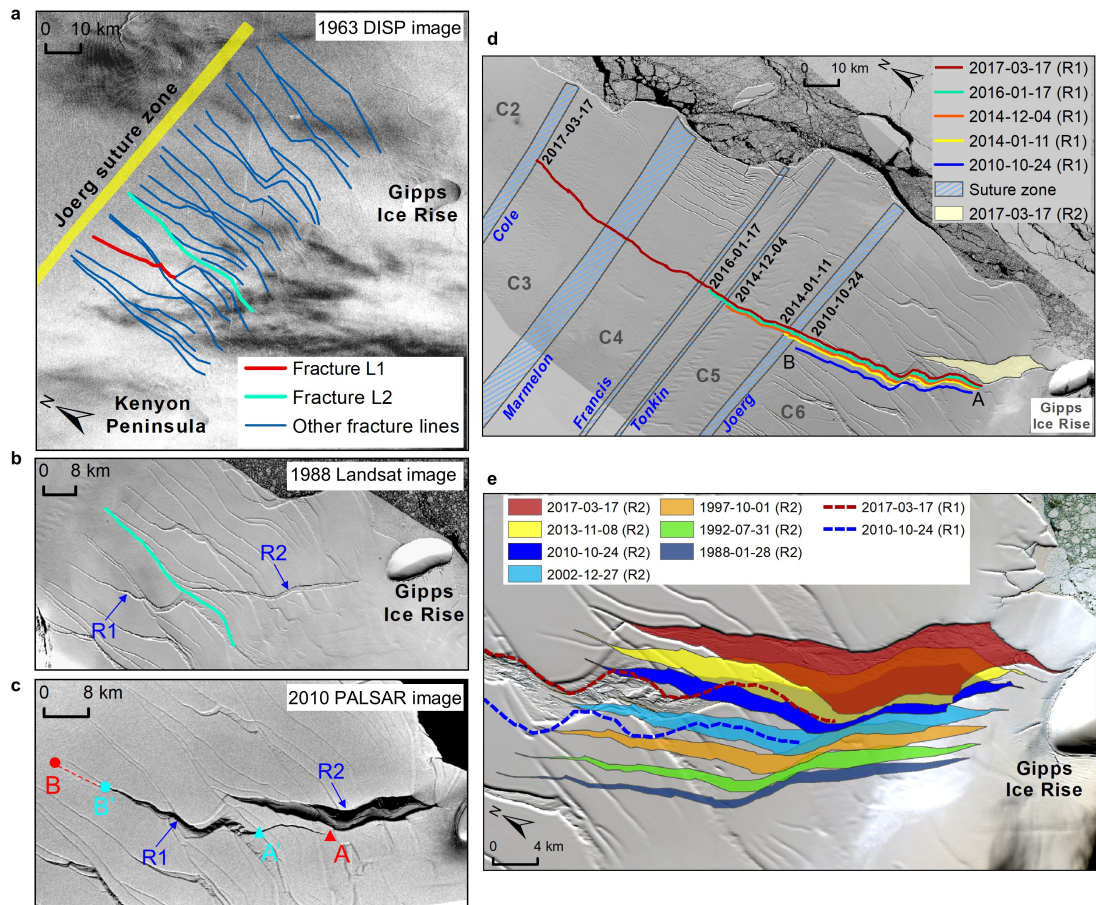


**Figure 2.** Development of two rifts that led to the 2017 calving event. **a.** Long and transverse fractures formed between Kenyon Peninsula and Gipps Ice Rise, delineated from the 1963 DISP imagery. **b.** The locations of R1 and R2 on the 1988 Landsat imagery. The cyan line corresponds to L2 in panel **a**. **c.** The locations of R1 and R2 on the 2010 PALSAR imagery, showing the widening of R2 and the propagation of R1 (from points A' to A and B' to B). **d.** The propagation of R1 from 2010 to 2017. **e.** The widening of R2 between 1988 and 2017 following the 1986 calving event that occurred at the southern ice front.

### 4.3 Temporal variability of flow velocity during 1963–2020

The earliest flow velocities were derived from the 1963 DISP imagery and the Landsat imagery acquired in 1986 and 1988. Since the available images for 1986 cannot fully cover Larsen C, we used the 1988 imagery to fill the data gaps. We also derived the 1986–1988 flow velocities for the area where both 1986 and 1988 images are available. Due to the limited resolution of the DISP imagery and the long-time span with the Landsat data, the flow velocities for this period (1963–1986/1988) are relatively sparse, and are distributed over the areas with large visible surface features (Figure 3a). Nevertheless, these velocity measurements still provide important baseline information for examining the long-term changes in ice flow. Figure 3b shows the temporal variability of flow velocity over five areas, including the upstream ice shelf (Area 1), the northern downstream portion (Area 2), the ice front near Bawden Ice Rise (Area 3), the central ice shelf (Area 4), and the southern downstream portion (Area 5). Before 1990, there was no significant velocity change across Larsen C. On average, the flow velocities after 2000 were higher compared to the velocities before 1990. Area 1 shows a gradual velocity increase between 2000 and 2016. Both Area 3 and Area 5 exhibit a step change in velocity ( $\sim 50$  m/year) between the 2000–2002 and 2008–2010 periods. The acceleration of Area 3 was related to the northern calving near Bawden Ice Rise in 2004/2005. The acceleration of Area 5 was concurrent with the rift propagation of R1 during 2006–2010. The 2017 calving event did not trigger an immediate flow speedup across the ice shelf.

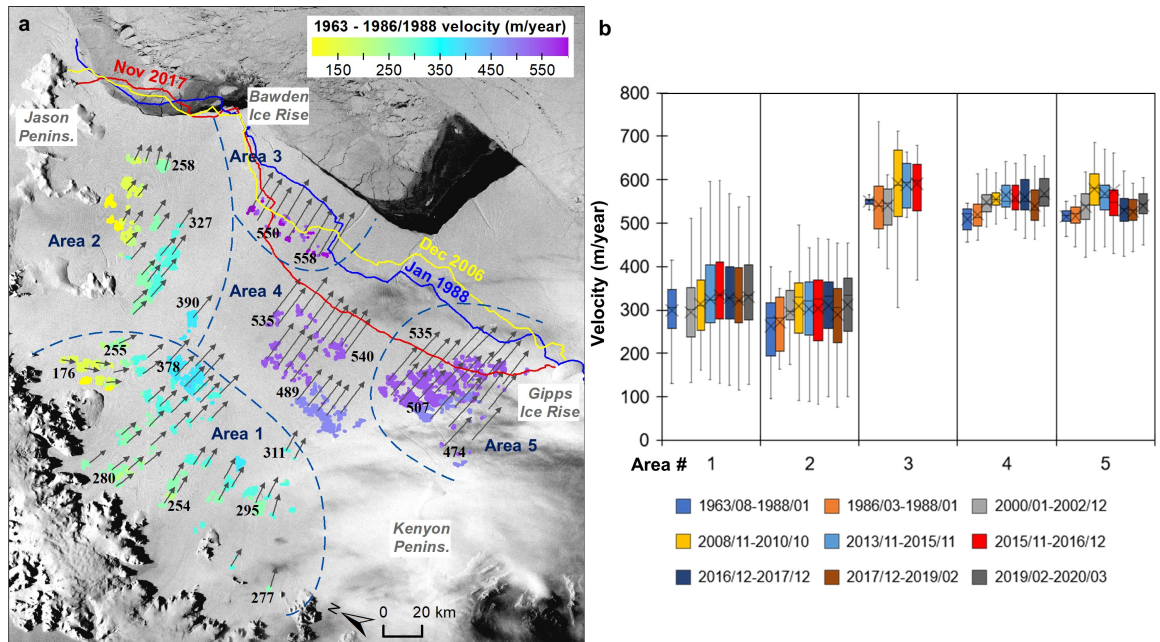


**Figure 3.** a. The 1963–1986/1988 flow velocities. The background image is the georeferenced DISP image showing the extended ice front in the south in 1963.

The dashed lines divide the velocity data into five regions (Areas 1–5). **b.** Box and Whiskers plots of the time-series flow velocities for the five areas, generated based on the velocity measurements of the locations where the 1963–1986/1988 velocity data are available for each period. The “x” markers indicate the mean value.

#### 4.4 Flow accelerations associated with rifting and calving

The most significant velocity change was strongly related to the rift development within the downstream portion of the C5–C6 units (Figure 4). There was a sharp velocity change along the rift line during 2015–2016 (Figure 4e) immediately before the calving occurred. Along the C6 flow line (Figure 4h), the average velocity of the portion that calved in 2017 increased by more than 50% from  $570 \pm 16$  m/year during 1986–1988 to  $890 \pm 36$  m/year during 2015–2016. The largest increase over this period was between 2013–2015 and 2015–2016, when the velocity increased by  $21.6 \pm 2.5\%$  from a speed value of  $731 \pm 25$  m/year. In comparison, the central ice shelf (C4; Figure 4g) exhibited much less variability in velocity before calving. The calved portion of C4 had an average velocity of  $723 \pm 21$  m/year during 2015–2016, increasing by only  $3.1 \pm 0.7\%$  relative to the previous period 2013–2015. However, there was a velocity increase of  $9.1 \pm 2.3\%$  between 1986–1988 and 2000–2002 from the ice front to an upstream distance of  $\sim 80$  km. This acceleration was very likely due to the velocity adjustment in response to the front geometry change caused by the 1986 retreat. Despite the sparse velocity data before 2000, this observed acceleration pattern may indicate a lagged response of flow velocity to front retreat. The lagged response suggests that although the 2017 calving event has not yet induced any significant flow accelerations, there is potential for a future flow velocity response to the 2017 event.

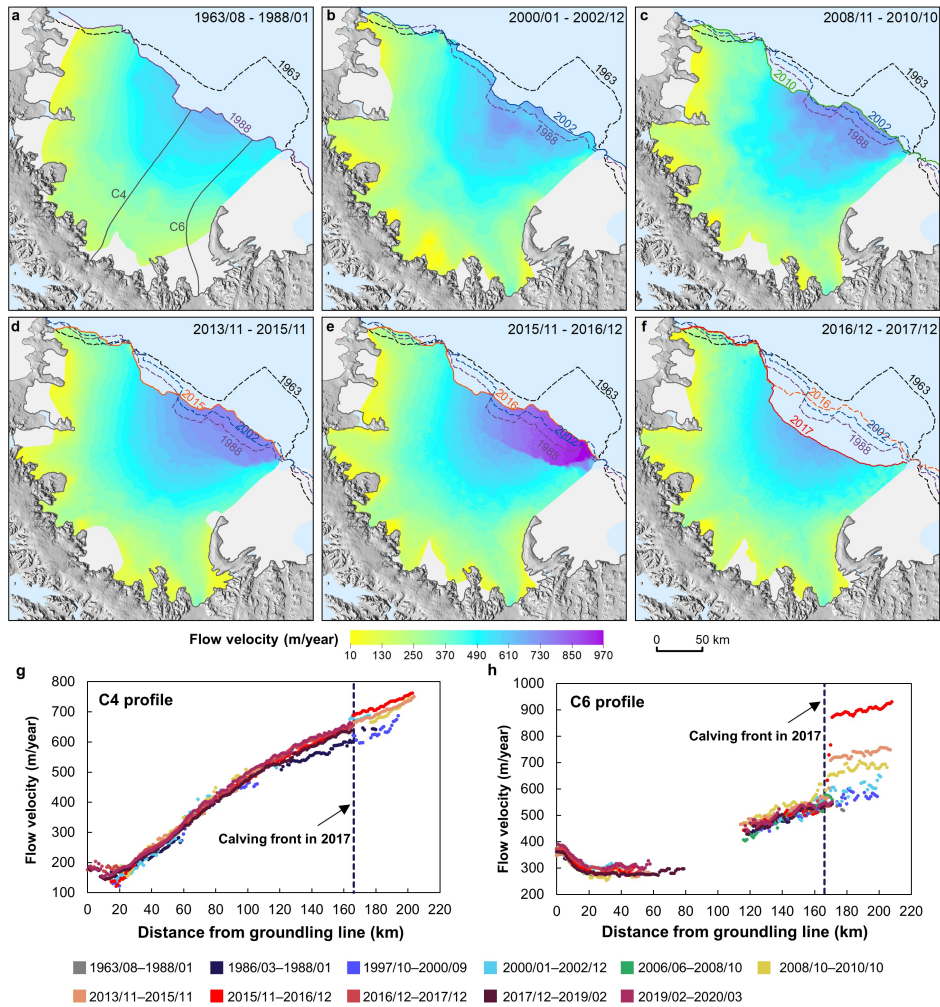


**Figure 4.** Flow velocity maps (a–f) of six selected periods with ice front changes, and along-flow velocity profiles for C4 (g) and C6 (h). The locations of the C4 and C6 centerlines are shown in panel a.

## 5 Modeling experiments

The observational data have indicated a clear but also complex linkage between ice shelf retreat, flow acceleration, and rift development. Both front geometry change and rift development modulate the stress conditions across the ice shelf, which in turn change flow velocities and strain rates, further affecting rift-ing and calving. We conducted diagnostic modeling experiments to investigate how varying front geometry and rift-induced weakening control the dynamic responses of ice shelf flow velocities and stress fields.

### 5.1 Ice rigidity inversion and modeling scenarios

Before the diagnostic experiments, we first solved for the ice rigidity  $\bar{B}$  using the inversion procedure in ISSM. We used the 450-m resolution MEaSUREs phase-based Antarctica ice velocity data product (Mouginot et al., 2019) to solve for  $\bar{B}$ . We used this velocity product to avoid uncertainties induced by velocity interpolation errors. This velocity product agrees best with the derived 2008–2010 flow velocities, with an average difference of  $10 \pm 25$  m/year. Figure 5a shows the optimized ice rigidity  $\bar{B}$ . This parameter defines the relationship between strain rate and stress, and is affected by ice temperature, fabric, water content, impurities and presence of cracks. Low values of  $\bar{B}$  indicate “soft” ice and high values indicate “stiff” ice. The spatial pattern of  $\bar{B}$  (Figure 5a) shows a good agreement with the suture zones and the zones of rapid shearing where outlet glaciers are flowing past promontories near the upglacier end of the ice shelf. The low values of  $\bar{B}$  near Gipps Ice Rise (highlighted area in Figure 5a) are due to the observed rift that mechanically weakened the ice shelf, thus making the ice appear “softer” than the surrounding ice. This results from the objective of parameter inversion, which is to minimize the difference between modeled and observed flow velocities under the continuum-mechanical modeling framework. When simulating for the years without rifting, these low values of  $\bar{B}$  derived from the rifted condition could artificially influence the model simulations. We modified the  $\bar{B}$  values in this rifted area (Figures 5b and c) for different modeling scenarios. We considered three scenarios as follows.

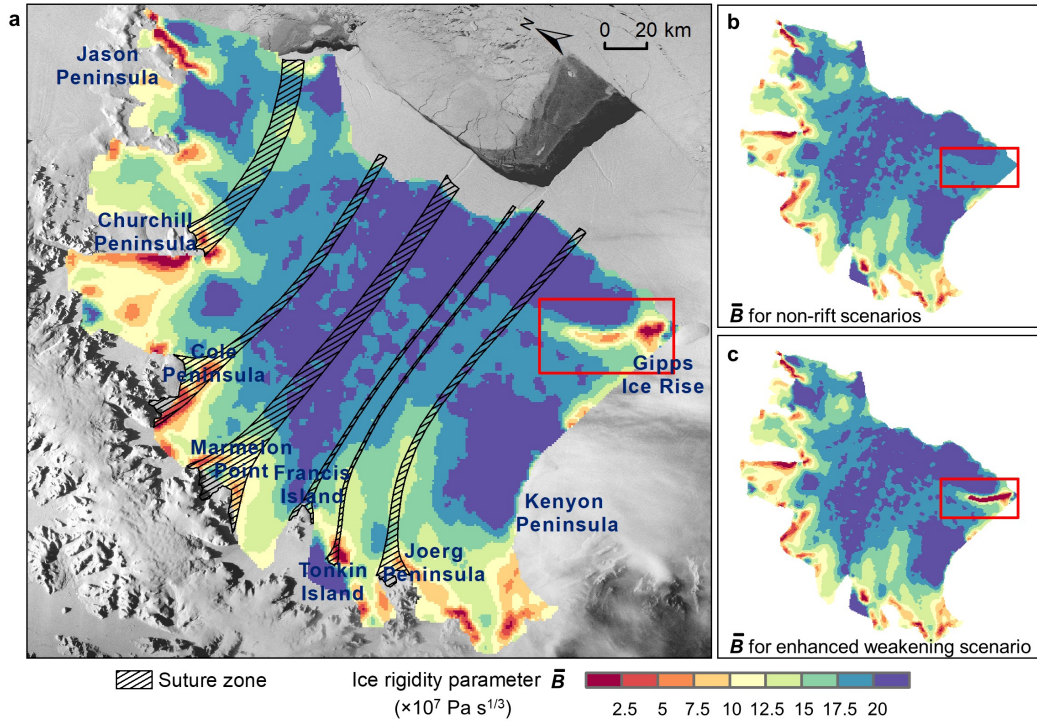


**Figure 5.** a. The optimized ice rigidity  $\bar{B}$  through inversion in ISSM. b. The

modified  $\bar{B}$  used for the non-rift scenario. **b.** The modified  $\bar{B}$  used for the enhanced weakening scenario.

**Non-rift scenario with different front geometry conditions.** This scenario aims to examine the dynamic responses of ice shelf velocity and stress to front geometry change. We controlled for rift effects by replacing the low values of  $\bar{B}$  near Gipps Ice Rise with the values of the adjacent intact areas (Figure 5b). We tested nine front geometry conditions (Figure 6), including four historical front locations (F1–F4), and five hypothetical front locations (H1–H5) under future retreat scenarios. H1–H5 were determined by assuming a radical retreat scenario, in which the new ice front reaches the compressive arch. The compressive arch is the boundary where the second principal stress changes from negative to positive, and has been used as a critical boundary to predict ice shelf instability (Doake et al., 1998; Kulesa et al., 2014). It has been suggested that ice shelf retreat will become irreversible once the ice front retreats behind the compressive arch. H1 (Figure 6e) is the front location where the retreat reaches the current compressive arch (shown in Figure 6d); H2 is the front location where the retreat reaches the compressive arch for the geometry condition H1, and similarly for H3. Once the ice front reaches H3 or exceeds H3, the compressive arch would no longer exist. H4 is the front condition if the H3 front continues retreating another 1 km, and H5 is the front condition if H4 keeps retreating by  $\sim 20$  km (Figure 6g). H4 and H5 were used to test how sensitive the ice shelf would be to changes in the ice shelf front when the compressive arch is absent.

**Rift-scenario 1 with original  $\bar{B}$ .** Through two rift scenarios, we aim to test the hypothesis based on the observations: the weakening due to the rift R2 was crucial for the propagation of R1, which resulted in the 2017 calving event. In this scenario, we used the original ice rigidity  $\bar{B}$  (Figure 5a), which includes, to a certain extent, the R2-induced weakening.

**Rift-scenario 2 with enhanced weakening.** We considered a weakening-enhanced scenario by further decreasing the rigidity  $\bar{B}$  to a minimum value of  $0.1 \times 10^8 \text{Pa s}^{1/3}$  over the rifted area (Figure 5c).

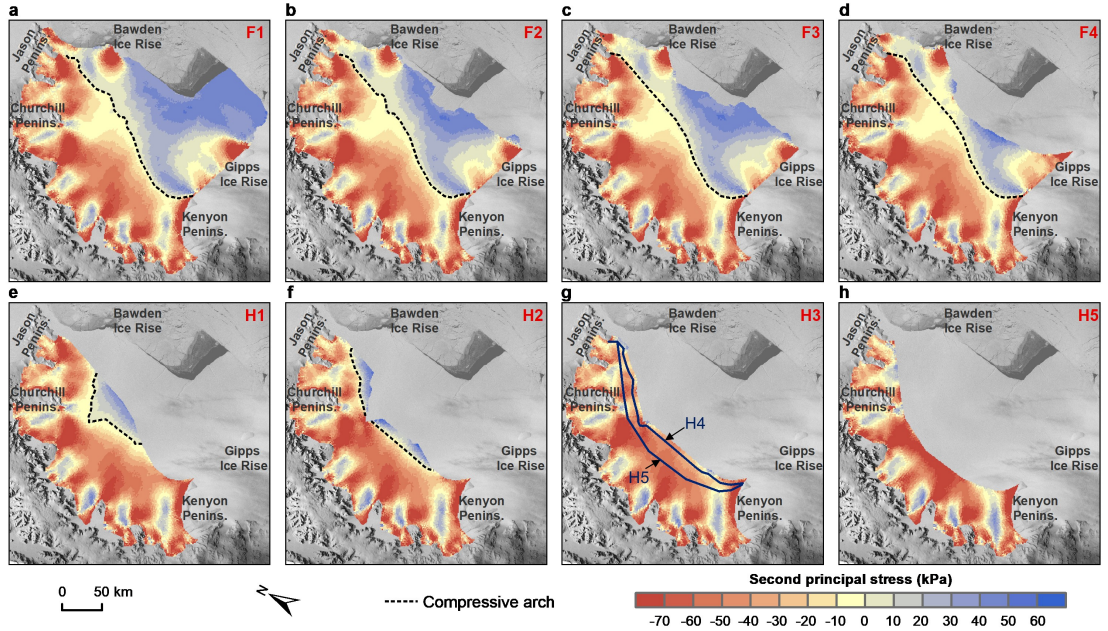


**Figure 6.** Second principal stresses and compressive arch locations for different front geometry conditions (non-rift scenario). F1–F4 are the front locations in 1963, 2000, 2013, and 2017, respectively. H1–H5 are the hypothetical front locations under future retreat scenarios.

### 5.2 Dynamic responses to front retreat (non-rift scenario)

The retreat events during 1963–2020 neither exceeded nor modified the compressive arch (Figures 6a–d). Under future retreat scenarios, successive retreat would allow the compressive arch to migrate upstream until H3 (Figures 6e, f). The front geometry change due to retreat can result in flow accelerations and backstress loss (Figure 7), with the magnitude and extent depending on the location of the retreat. The two retreat cycles reduced the backstress at the areas adjacent to the ice rises and the central downstream portion (Figure 7i–k). Flow accelerations (greater than 20 m/year) caused by front geometry change are limited to the central downstream portion and are less than 50 m/year for the majority of Larsen C (Figures 7a–c). Therefore, the front geometry change due to the past retreat events is insufficient by itself to explain the observed velocity increase. We compared the derived flow velocities with the modeled flow velocities of corresponding front geometry. Over the downstream portion of the ice shelf, the averaged difference increases over time with the propagation of R1 and R2 from  $9.8 \pm 8.5\%$  (2000–2002, F2 condition), to  $16.3 \pm 8.6\%$  (2008–2010, F3 condition), to  $17 \pm 12.9\%$  (2013–2015, F3 condition), and to  $23.4 \pm 24.5\%$  (2015–2016, F3 condition). This suggests that, to make a realistic prediction of flow velocity change due to ice shelf retreat, it is necessary to first consider rift development in response to front retreat. Nevertheless, the modeling scenario

considering only the front geometry condition can be used with the observational data as a diagnostic indicator. The increasing difference between observed and modeled flow velocities over time may be an indicator for future calving events.

However, even without considering rifts, once the ice front reaches the current compressive arch, widespread flow accelerations (~25%) would be triggered (Figure 7d), as a result of the dramatic backstress loss (Figure 7l) from Bawden Ice Rise and Gipps Ice Rise. This emphasizes the important role of ice rises in stabilizing the ice shelf. Complete buttressing loss from ice rises would cause ice-shelf-wide flow accelerations, and the backstress-reducing effect would extend to the grounding line. After the compressive arch ceases to exist, even small perturbations in the ice front would cause large-scale backstress loss and flow accelerations (Figures 7g–h, o–p), particularly over the C2 and C6 units. This effect would reach the grounding line, and the upstream glaciers feeding the C2 and C6 units would speed up in response to the buttressing loss caused by a small retreat at the ice front. This scenario resembles the pre-collapsed Larsen B, for which the compressive arch was removed and flow accelerations occurred across the ice shelf. These modeling experiments suggest that ice rises are crucial for determining the tipping point of ice shelf stability. The compressive arch is the critical boundary, beyond which the ice shelf flow velocities and stresses are highly sensitive to front retreat. Once the compressive arch is absent, front geometry change will become an important control on ice shelf flow dynamics and stress conditions.

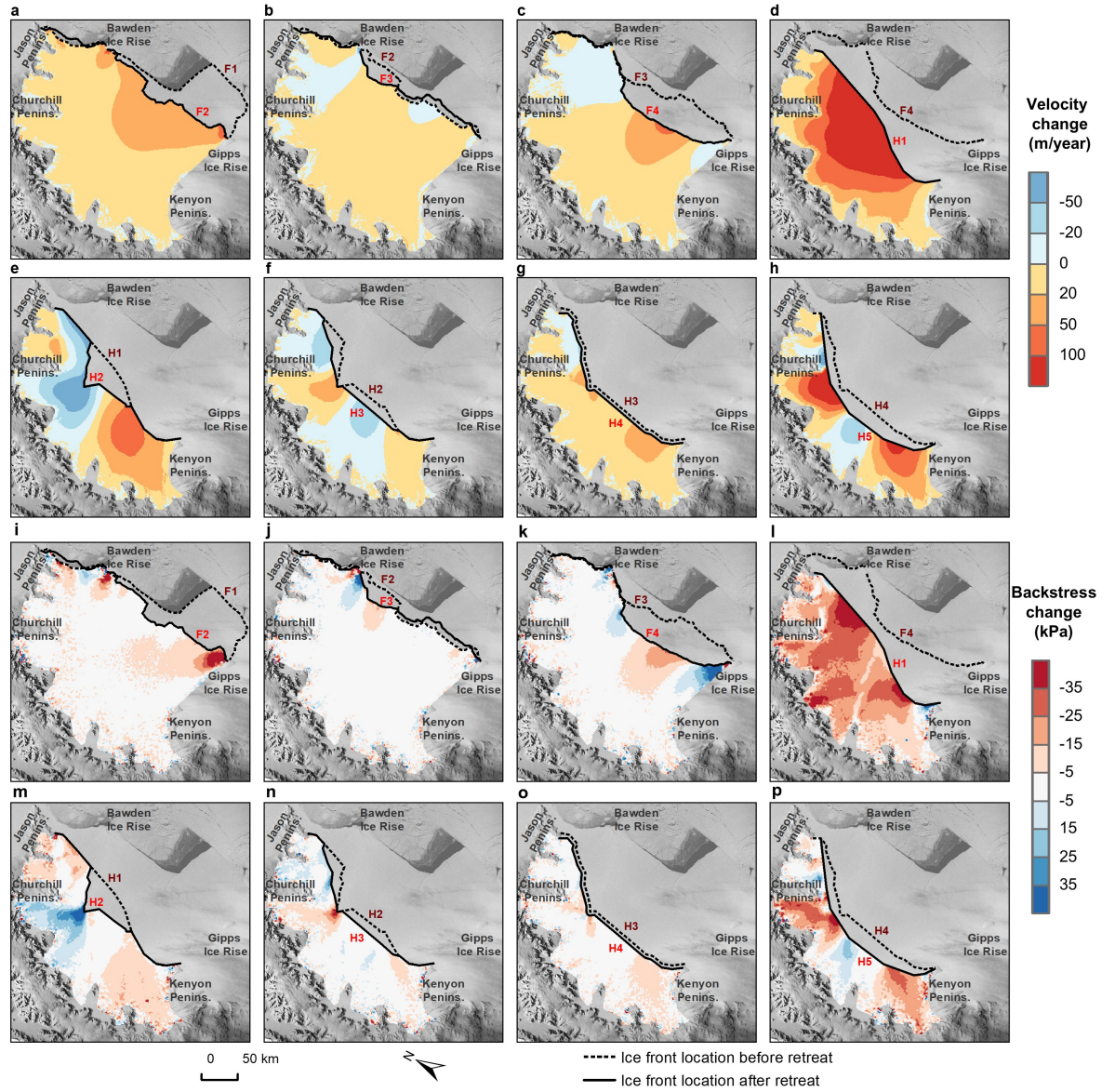


**Figure 7.** Changes of modeled flow velocities (a–h) and backstresses (i–p) in response to the front geometry changes (non-rift scenario).

### 5.3 Longitudinal deviatoric stress field and rift opening (non-rift scenario)

We find that the modeling scenario considering only the front geometry condition is also useful to diagnostically predict the rift opening location. Figures 8a–b show the longitudinal deviatoric stress fields for F2 (2000 front) and F3 (2013 front), with positive values representing tensile conditions along the flow

direction and negative values for compressive conditions. The locations where rifts opened strongly coincided with the transitional zone from compressive to tensile longitudinal conditions, including the rift near Bawden Ice Rise (Figure 8c) that caused the northern calving event in 2004/2005, and the rift R2 (Figure 8d) whose expansion to Gipps Ice Rise directly related to the rift R1 and eventually caused the 2017 calving event. This transitional pattern appears to be a characteristic feature near ice rises. Although we did not account for the rift-induced weakening effect on ice rigidity, the longitudinal deviatoric stress field may be used as an important diagnostic feature to identify potentially vulnerable areas that are favorable for rift opening, especially within the transitional zone from compressive to tensile conditions. Identifying the potential locations of the initial rift opening is a necessary step for introducing rift-caused damage into ice shelf models.

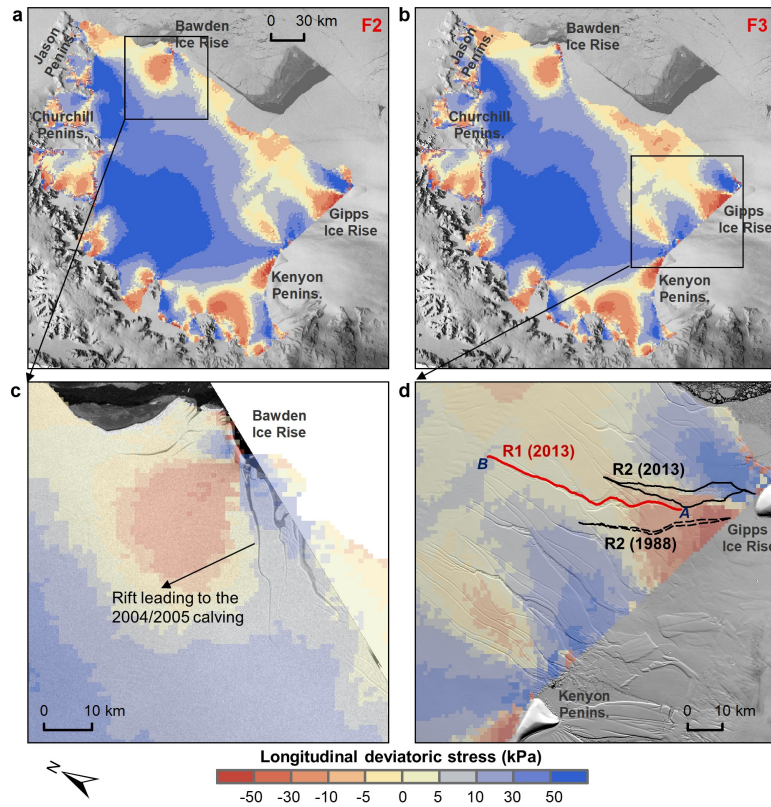


**Figure 8.** Longitudinal deviatoric stress fields for geometry conditions F2 (panels a and c, ice front in 2000) and F3 (panels b and d, ice front in 2013). The background image in panel c is the Envisat ASAR image acquired on August 03, 2004, showing the rift causing the northern calving event. The background image in panel d is the Landsat-8 OLI panchromatic image acquired on January 11, 2014, showing the expansion of R2 to Gipps Ice Rise.

#### 5.4 Impact of rift-induced weakening (rift scenarios)

The modeling results of rift scenarios indicate the R2-induced weakening near Gipps Ice Rise was critical to the propagation of R1. If the weakening effect of R2 is not considered, the southern rift tip ('A') of R1 would be in a compressive longitudinal condition (Figure 8d). Once the R2-induced weakening is incorporated (Figure 9b), the southern rift tip ('A') would be in a tensile longitudinal condition that is favorable for rift growth. This suggests that R1 would be less likely to propagate towards the south if the ice shelf were not damaged by R2 near the ice rise. Based on satellite images, R1 almost reached R2 in 2010 (Figure 2c), which further weakened the area. The continued weakening can further enhance the longitudinal stretching over an expanded area for both rift scenarios (Figures 9e, h), indicating that this weakening could promote the subsequent northward propagation of R1.

We also analyzed the first principal stresses (Figure 10). The first principal stress is the maximum value of stress that is normal to the plane in which the shear stress is zero. Therefore, it indicates the magnitude and orientation of the maximum tensile stress. Fractures tend to open along the direction of the first principal stress, and the opening rate would be maximized if the flow direction is along the first principal axis (e.g., Benn et al., 2007; Colgan et al., 2016; Kulesa et al., 2014). The angle between the first principal axis and flow direction (stress-flow angle) can be used to evaluate rift propagation and ice shelf stability (Kulesa et al., 2014). A small stress-flow angle would be more likely to promote rift propagation than a large angle. The rift-induced weakening would modify the stress-flow angles (Figures 10a-c) along the trajectory of R1 to more favorable conditions for rift propagation. The magnitude of first principal stresses would also increase in response to the rift-induced weakening (Figure 10d-f). The northern rift tip ('B') of R1 reached an area with stress-flow angles of less than 10 degrees after January 2016, which could explain the rapid propagation of R1 afterwards. The path of rift tip 'B' growth was perpendicular to the flow direction. Once the rift tip was in the area where the first principal axis was aligned with the flow direction, the rift growth was unstoppable until it reached the area where the stress-flow angles were greater than 30 degrees. Therefore, the rift-induced weakening could increase both longitudinal stresses and first principal stresses and modify the stress-flow angles nearby, resulting in favorable stress conditions for the rift (R1) propagation towards the north. The opening of R2 therefore preconditioned the R1 growth and the 2017 calving event.

The modeling results also indicate the rift-induced weakening caused the localized flow accelerations at the downstream portion of southern Larsen C. The flow velocity increases near Gipps Ice Rise as compared to the non-rift scenario are shown in Figure 9d. With the further enhanced weakening, the acceleration increases both upstream and downstream of the rifted location (Figure 9g). This is consistent with the observed spatial pattern of velocity increase (Figure 4). The rift development can also reduce the ice shelf backstress (Figures 9c, f,

i), although the magnitude and extent of backstress loss depend on how much weakening is caused by rifts. With enhanced weakening, the backstress loss can extend upstream and potentially reach the grounding line. This suggests that rift propagation needs to be considered for evaluating the buttressing change of ice shelves.

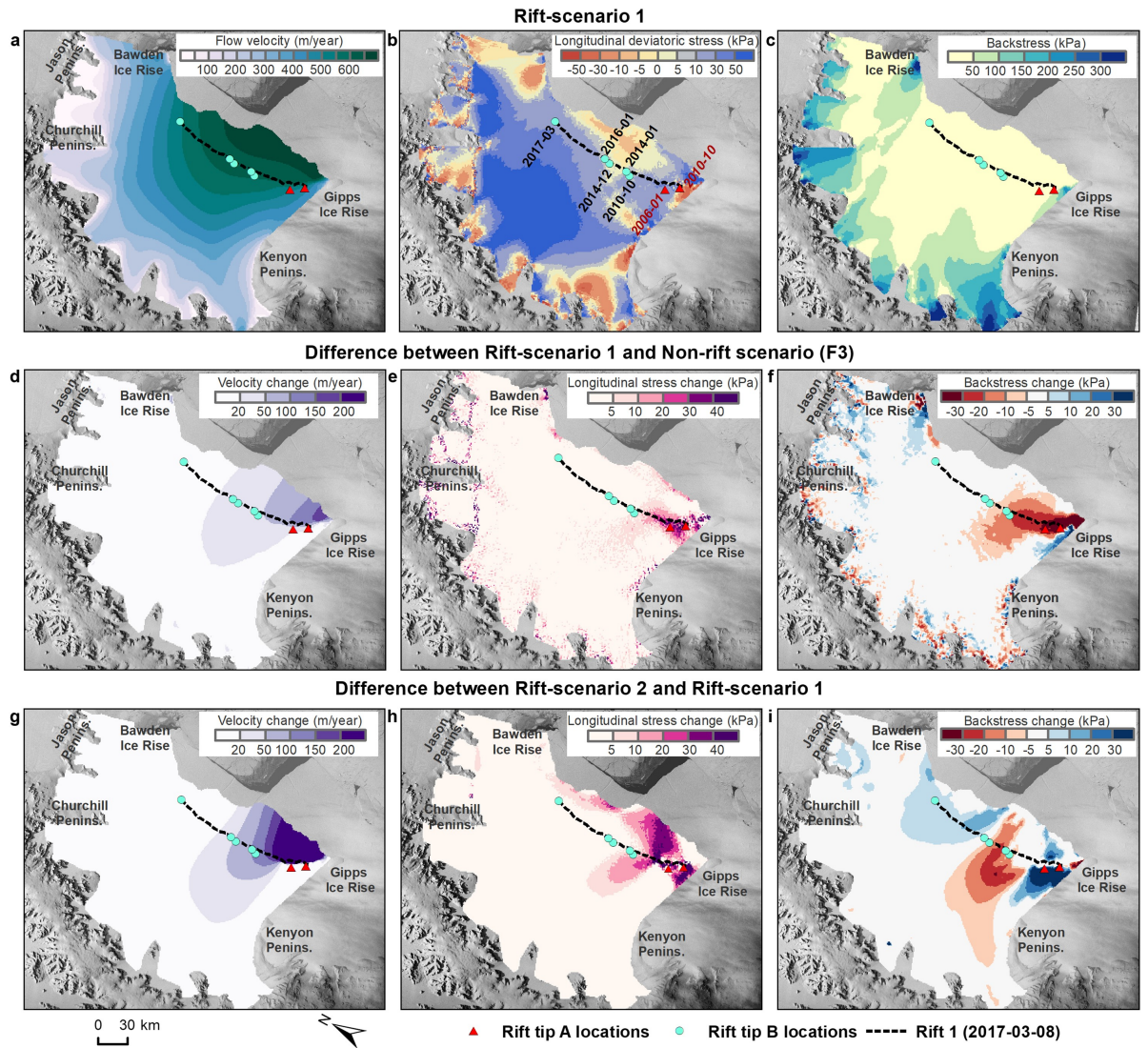


**Figure 9.** Modeled flow velocity (a), longitudinal deviatoric stress (b), and backstress (c) for rift-scenario 1. Differences of these quantities between rift-scenario 1 and non-rift scenario (d-f), and between rift-scenario 2 and rift-scenario 1 (g-i).

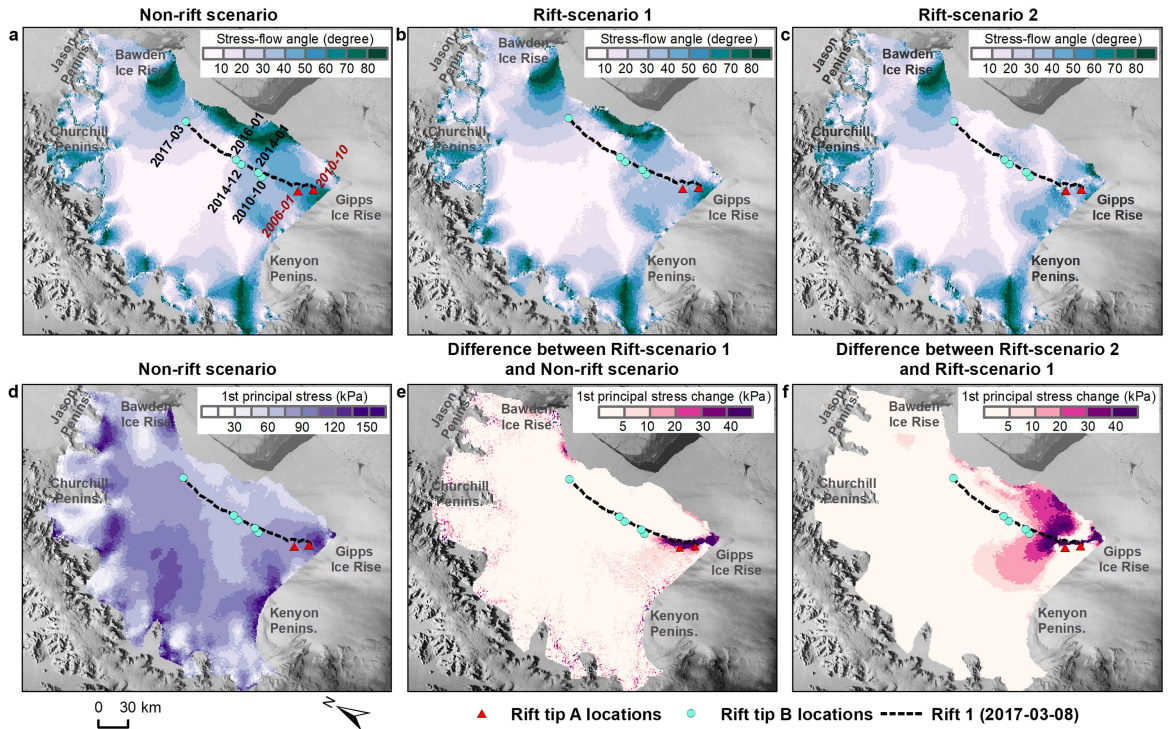


**Figure 10.** Stress-flow angles for non-rift scenario (a), rift-scenario 1 (b), and rift-scenario 2 (c, enhanced weakening). First principal stress field for non-rift scenario (d), and differences between rift-scenario 1 and non-rift scenario (e), and between rift-scenario 2 and rift-scenario 1 (f). The extent of R1 is shown (dashed line) with the rift tip locations between 2006 and 2017.

## 6 Discussion

The multidecadal satellite data and modeling experiments indicate the primary role of rifting processes in controlling the retreat of Larsen C over the past six decades. The two retreat cycles were characterized by tabular iceberg calving due to rift propagation. The rifts leading to calving developed near the Bawden Ice Rise in the north and the Gipps Ice Rise in the south. The time series of satellite data allowed us to analyze the rifting processes causing the 2017 calving event in a high level of detail. The 2017 calving event resulted from the propagation of two rifts, including a transverse rift (R1) formed downstream of Kenyon Peninsula and an oblique rift (R2) formed near Gipps Ice Rise. The observed flow accelerations were mainly related to the propagation of these two rifts. Enhanced weakening due to R2 near Gipps Ice Rise increased both longitudinal and first principal stresses around R1, and modified the stress-flow angles, creating favorable conditions for the northward propagation of R1. This indicates the importance of considering feedbacks between different rifts. Several studies (e.g., Borstad et al., 2017; Jansen et al., 2015) discussed the rift

development causing the 2017 calving event, but treated R1 and R2 as one single rift and mainly focused on the northward propagation. Our results suggest that the southward propagation of both R1 and R2 preconditioned the northward propagation.

According to linear elastic fracture mechanics (LEFM), a fracture propagates when the stress intensity factor at a crack tip exceeds the material fracture toughness (Hulbe et al., 2010; Lipovsky, 2020). At the fracture tip, the stress intensity factor is determined by fracture geometry, fracture length, and stress field. The stress intensity factor has three modes: Mode I–opening (tensile), Mode II–sliding (in-plane shear), and Mode III–tearing (antiplane shear). The propagation of R1 was dominated by Mode I. Fracture propagation continues until the stress intensity factor is less than the fracture toughness. Suture zones are suggested to have resistive effect on rift propagation because of the high fracture toughness of marine ice underneath (Borstad et al., 2017; Kulessa et al., 2019; McGrath et al., 2014). Marine ice has different material properties from meteoric ice originating from glacial ice, and was detected underneath the Larsen C suture zones (Holland et al., 2009; Jansen et al., 2013). Assuming that the spatial distribution of fracture toughness is fixed, the increased tensile stresses at the crack tips of R1 are necessary conditions to activate the propagation of R1. The modeling results indicate the R2-induced weakening near Gipps Ice Rise caused the enhanced tensile stresses around R1, highlighting the importance of rift features around ice rises. Meanwhile, reduced fracture toughness of suture zones due to ice shelf thinning should also be considered. Widespread thinning has been observed over Antarctic ice shelves from satellite altimetry data (Adusumilli et al., 2020), including Larsen C (Adusumilli et al., 2018; Shepherd et al., 2003). The surface lowering of Larsen C has been attributed to multiple factors, including firn compaction, ice divergence due to flow acceleration, and basal melt (Holland et al., 2015; Shepherd et al., 2003). A high basal melt rate was observed near Bawden Ice Rise (Adusumilli et al., 2018). Ocean-driven melting underneath Larsen C can enhance the rifting processes by 1) reducing marine ice underneath the suture zones, decreasing the fracture toughness of suture zones; 2) destabilizing the ice rises and reducing the buttressing force from ice rises (Borstad et al., 2013); and 3) thinning and weakening shear margins (Alley et al., 2019; Dow et al., 2018; Lhermitte et al., 2020).

To better predict ice shelf retreat due to rifts, we not only need to know whether a rift would propagate until calving occurs, but also where rifts tend to initiate. Rifts initiate at preexisting cracks or flaws (Hulbe et al., 2010). A recent study based on ICESat-2 data (Wang et al., 2021) found that the vertical depth of preexisting fracture features is critical for predicting rift locations. Theoretical modeling studies (e.g., Lipovsky 2020) suggest that the loss of marginal strength, when ice flows out of an embayment, can trigger rift growth. Our modeling results (Figure 8) suggest that the transitional area from a compressive (longitudinal) condition to a tensile (longitudinal) condition resulting from ice shelf geometry conditions is also a potential location for rift initiation and

opening. There were three such transitional areas at the downstream portion of Larsen C, including the area near Bawden Ice Rise, the area near Gipps Ice Rise, and the area downstream of Kenyon Peninsula. Satellite images showed that the rifts causing the northern and southern calving events were initiated in these areas. The area downstream of Kenyon Peninsula is a typical transitional area from strong to weak shear margins, consistent with the modeling study of Lipovsky (2020). The transitional areas can be identified through diagnostic modeling given a front geometry condition without considering ice shelf damage. Once a rift is initiated, the rift-induced weakening must be incorporated to examine whether the rift will propagate in response to the modification of stress field. The weakening is enhanced when the rift growth continues, further altering the stress field. Therefore, it is important to capture the time-varying effect of rifts on ice rigidity in ice flow models. Capturing such feedbacks appears to be essential for modeling flow velocity fields and subsequent rift propagation. Continuum damage mechanics (Borstad et al., 2012, 2013; Krug et al., 2014) have been recently utilized to incorporate fracture-induced weakening into a viscous continuum damage model. The damage factor is a scalar variable that is quantified by an inversion (ice rigidity) approach. In this case, damage-related flow velocities are required to invert for the damage factor. Further investigation into the temporal evolution of rift length and associated damage is needed to enable parameterization of these processes within a modeling framework.

The velocity data indicate that the impact of the 2017 calving event is limited on the ice shelf flow dynamics. The calved portion was located in the “passive ice” zone (Fürst et al., 2016; Reese et al., 2017), where the front retreat has little effect on ice shelf buttressing. We observed flow accelerations in the central ice shelf after 2000, which might be a velocity adjustment to the front geometry change resulting from the calving events before 1990. The modeling experiments (Figures 7c, 7k) show the front geometry change due to the 2017 calving would increase the velocity (although at a low magnitude) and decrease the backstress in the central ice shelf, suggesting a potential time-lag between front retreat and ice shelf flow acceleration. If the retreat continues and the ice front reaches the compressive arch, widespread flow accelerations will be triggered due to front retreat. The observed flow accelerations were mainly caused by the rift development in the south. To predict future ice shelf flow dynamics due to front retreat, rift initiation and propagation and associated weakening effect on ice rigidity should be considered for modeling flow velocity fields.

Following the disintegration of Larsen A and Larsen B, one pressing question is whether Larsen C will disintegrate in the same manner. The collapses of Larsen A and Larsen B were preceded by extensive surface melt, and hydrofracturing has been the prevailing hypothesis for explaining the ice shelf collapse (e.g., van den Broeke, 2005; MacAyeal et al., 2003). Abundant meltwater, surface fractures, and favorable stress conditions are the necessary elements of hydrofracturing. Lai et al. (2020) applied LEFM and assessed the vulnerability to hydrofracturing across all Antarctic ice shelves, in which Larsen C was classified as vulnerable to hydrofracturing. However, it is still questionable whether there

will be sufficient meltwater to fill the crevasses on Larsen C. Although several studies indicated that foehn wind enhances the surface melt rate over Larsen C (Datta et al., 2019; Elvidge et al., 2020; King et al., 2017), the extent of ponded water is limited in space, mostly occurring at the northern upstream portion at the Cabinet Inlet (C3 unit). Besides excessive melt occurred on Larsen A and Larsen B, their pre-collapse front geometries were already in unstable conditions after the compressive arch was reached (Doake et al., 1998). Larsen C will resemble the pre-collapse Larsen B if the front geometry reaches the position of H3 and the compressive arch is absent (Figure 6). The disintegration of Larsen C is less likely to occur in the current condition. However, given the importance of rifting processes to the stability of Larsen C, it is critical to monitor how atmospheric warming and oceanic forcing will affect rifting processes in the future.

## 7 Conclusions

We combined multi-source satellite data over the past six decades to investigate changes occurring over the Larsen C ice shelf. The total ice shelf area was reduced by more than 20% from 1963 to 2020, as a result of two large retreat cycles. Each cycle was characterized by a northern retreat near Bawden Ice Rise followed by a southern retreat near Gipps Ice Rise, in which rifting-induced tabular iceberg calving was the dominant mechanism. We analyzed the temporal evolutions of two rifts that caused the 2017 calving event in the south, and found their close interactions in weakening the ice shelf. In particular, the weakening due to R2 near Gipps Ice Rise preconditioned the rapid propagation of the major rift R1. We observed a lagged response of flow acceleration to front retreat, which leads to our conjecture that there will be a gradual velocity increase in response to the 2017 calving event, despite relatively small recent changes. The ice shelf retreat away from pinning points (ice rises) to the location of compressive arch will reduce the ice shelf backstress and lead to widespread flow accelerations. When the compressive arch ceases to exist, small retreat events can trigger large-scale backstress loss and flow accelerations extending to the upstream glaciers.

The results of this study in combination with observations of the pre-collapsed Larsen B suggest a chronology of ice shelf destabilization processes for embayment-confined ice shelves. Rifts initiate at preexisting cracks and/or areas with favorable stress conditions, such as the transitional area from compressive to tensile longitudinal conditions. Ice rises and locations with a transition from strong lateral shear margins to weak margins (e.g., occurring near an island or peninsula) generally have such characteristic stress patterns. Rifts would propagate at these transition areas, if the stress intensity at the crack tips exceeds the fracture toughness. Rift growth leads to mechanical weakening of ice and a change in ice rigidity property. The weakening, particularly near ice rises and/or shear margins, results in flow accelerations, further modifies the stress field by increasing longitudinal stretching and decreasing stress-flow angles, hence creates more favorable conditions for rift propagation, and eventually causes ice front retreat. If the front retreat occurs

within the “passive ice” area and does not extend to the compressive arch, a limited or lagged response in flow velocity and stress field would be triggered. If the front retreats behind the compressive arch, widespread flow accelerations and backstress loss would be triggered, causing dynamic thinning and stress field change across the ice shelf. The compressive arch location may move further upstream or become fully absent. The absence of a compressive arch would create an unstable front condition, followed by persistent front retreat. If surface melting and ponding are prevalent due to atmospheric warming, hydrofracturing can destabilize the ice shelf rapidly. Oceanic forcing can affect this process by thinning shear margins and reducing marine ice underneath suture zones, both of which lower the fracture toughness and therefore enhance weakening and fracturing. Our results emphasize the need for capturing key processes in ice shelf evolution models. In particular, the response of the ice shelf mechanical strength to the presence of rifts and the feedbacks that can accelerate ice shelf retreat need to be incorporated in the models.

#### Acknowledgments

This research was supported in part by a Seed Grant award from the Institute for Computational and Data Sciences at the Pennsylvania State University. Part of the work was supported by the University of Cincinnati Graduate School Dean’s Fellowship when S. Wang was a graduate student. The authors acknowledge the United States Geological Survey (USGS) for the Declassified Intelligence Satellite Photography and Landsat images, the Alaska Satellite Facility for the ALOS PALSAR images, the European Space Agency for the ERS-1/2 and Envisat SAR images, the Byrd Polar and Climate Research Center at Ohio State University for the orthorectified Radarsat-1 SAR images and other RAMP data products, the National Snow and Ice Data Center for the Antarctic DEM data and the MEaSURES phase-based Antarctica ice velocity data, and the Jet Propulsion Laboratory and University of California at Irvine for the Ice-sheet and Sea-level System Model (ISSM).

There are no restrictions to access the data used for this study. The DISP imagery (<https://doi.org/10.5066/F78P5XZM>), Landsat-4/5 TM (<https://doi.org/10.5066/F7N015TQ>), Landsat-7 ETM+ (<https://doi.org/10.5066/F7WH2P8G>), and Landsat-8 OLI (<https://doi.org/10.5066/F71835S6>) images were downloaded from the USGS EarthExplorer data portal (<https://earthexplorer.usgs.gov/>), courtesy of the U.S. Geological Survey. The ALOS PALSAR images (© JAXA/METI ALOS PALSAR L1.5 2006-2010. Accessed through ASF DAAC 1 February 2014) were downloaded from the Alaska Satellite Facility data portal (<https://asf.alaska.edu/>). The Radarsat Antarctic Mapping Project (RAMP) data (<https://doi.org/10.5067/HHK2QT3LQMEL>) are available at <https://asf.alaska.edu/data-sets/derived-data-sets/ramp/ramp-get-ramp-data/>. ERS-1/2 SAR images were accessed from [https://earth.esa.int/eogateway/catalog/ers-1-2-sar-im-l0-sar\\_im\\_\\_0p-](https://earth.esa.int/eogateway/catalog/ers-1-2-sar-im-l0-sar_im__0p-), and Envisat ASAR images were accessed from [https://earth.esa.int/eogateway/catalog/envisat-asar-im-precision-l1-asa\\_imp\\_1p-](https://earth.esa.int/eogateway/catalog/envisat-asar-im-precision-l1-asa_imp_1p-), courtesy of European Space Agency. The DEM

data were accessed from the National Snow and Ice Data Center (<https://nsidc.org/data/nsidc-0082> and <https://nsidc.org/data/NSIDC-0422/versions/1>) (Liu et al., 2001; Bamber et al., 2009). The MEaSUREs phase-based Antarctica ice velocity data are available at <https://nsidc.org/data/NSIDC-0754/versions/1> (Mouginot et al., 2019b). The Ice-sheet and Sea-level System Model (ISSM) is open source and publicly available at <https://issm.jpl.nasa.gov/> (Larour et al., 2012).

#### References

- Adusumilli, S., Fricker, H. A., Siegfried, M. R., Padman, L., Paolo, F. S., & Ligtenberg, S. R. M. (2018). Variable Basal Melt Rates of Antarctic Peninsula Ice Shelves, 1994-2016. *Geophysical Research Letters*, *45*(9), 4086–4095. <https://doi.org/10.1002/2017gl076652>
- Adusumilli, S., Fricker, H. A., Medley, B., Padman, L., & Siegfried, M. R. (2020). Interannual variations in meltwater input to the Southern Ocean from Antarctic ice shelves. *Nature Geoscience*, *13*(9), 616–620. <https://doi.org/10.1038/s41561-020-0616-z>
- Alley, K. E., Scambos, T. A., Anderson, R. S., Rajaram, H., Pope, A., & Haran, T. M. (2018). Continent-wide estimates of Antarctic strain rates from Landsat 8-derived velocity grids. *Journal of Glaciology*, *64*(244), 321–332. <https://doi.org/10.1017/jog.2018.23>
- Alley, K. E., Scambos, T. A., Alley, R. B., & Holschuh, N. (2019). Troughs developed in ice-stream shear margins precondition ice shelves for ocean-driven breakup. *Science Advances*, *5*(10), eaax2215.
- Bamber, J. L., Gomez-Dans, J. L., & Griggs, J. A. (2009). Antarctic 1 km Digital Elevation Model (DEM) from Combined ERS-1 Radar and ICESat Laser Satellite Altimetry, Version 1. [Antarctic Peninsula]. Boulder, Colorado USA. NASA National Snow and Ice Data Center Distributed Active Archive Center. doi: <https://doi.org/10.5067/H0FQ1KL9NEKM>. [Date Accessed: 2019-01-01].
- Banwell, A. F., MacAyeal, D. R., & Sergienko, O. V. (2013). Breakup of the Larsen B Ice Shelf triggered by chain reaction drainage of supraglacial lakes. *Geophysical Research Letters*, *40*(22), 2013GL057694.
- Bell, R. E., Chu, W., Kingslake, J., Das, I., Tedesco, M., Tinto, K. J., et al. (2017). Antarctic ice shelf potentially stabilized by export of meltwater in surface river. *Nature*, *544*(7650), 344–348.
- Benn, D. I., Warren, C. R., & Mottram, R. H. (2007). Calving processes and the dynamics of calving glaciers. *Earth-Science Reviews*, *82*(3), 143–179.
- Bevan, S., Luckman, A., Hendon, H., & Wang, G. (2020). The 2020 Larsen C Ice Shelf surface melt is a 40-year record high. *The Cryosphere*, *14*(10), 3551–3564.
- Borstad, C., McGrath, D., & Pope, A. (2017). Fracture propagation and stability of ice shelves governed by ice shelf heterogeneity. *Geophysical Research*

*Letters*, 44(9), 4186–4194.

Borstad, C. P., Khazendar, A., Larour, E., Morlighem, M., Rignot, E., Schodlok, M. P., & Seroussi, H. (2012). A damage mechanics assessment of the Larsen B ice shelf prior to collapse: Toward a physically-based calving law. *Geophysical Research Letters*, 39(18), L18502.

Borstad, C. P., Rignot, E., Mouginot, J., & Schodlok, M. P. (2013). Creep deformation and buttressing capacity of damaged ice shelves: theory and application to Larsen C ice shelf. *The Cryosphere*, 7(6), 1931–1947.

van den Broeke, M. (2005). Strong surface melting preceded collapse of Antarctic Peninsula ice shelf. *Geophysical Research Letters*, 32(12), L12815.

Colgan, W., Rajaram, H., Abdalati, W., McCutchan, C., Mottram, R., Mousavi, M. S., & Grigsby, S. (2016). Glacier crevasses: Observations, models, and mass balance implications. *Reviews of Geophysics*, 54(1), 119–161.

Cook, A. J., Fox, A. J., Vaughan, D. G., & Ferrigno, J. G. (2005). Retreating glacier fronts on the Antarctic Peninsula over the past half-century. *Science*, 308(5721), 541–544.

Cuffey, K. M., & Paterson, W. S. B. (2010). *The Physics of Glaciers*. Academic Press.

DeConto, R. M., Pollard, D., Alley, R. B., Velicogna, I., Gasson, E., Gomez, N., et al. (2021). The Paris Climate Agreement and future sea-level rise from Antarctica. *Nature*, 593(7857), 83–89.

Depoorter, M. A., Bamber, J. L., Griggs, J. A., Lenaerts, J. T. M., Ligtenberg, S. R. M., van den Broeke, M. R., & Moholdt, G. (2013). Calving fluxes and basal melt rates of Antarctic ice shelves. *Nature*, 502(7469), 89–92.

Doake, C. S. M., & Vaughan, D. G. (1991). Rapid disintegration of the Wordie Ice Shelf in response to atmospheric warming. *Nature*, 350(6316), 328–330.

Doake, C. S. M., Corr, H. F. J., Rott, H., Skvarca, P., & Young, N. W. (1998). Breakup and conditions for stability of the northern Larsen Ice Shelf, Antarctica. *Nature*, 391(6669), 778–780.

Dow, C. F., Lee, W. S., Greenbaum, J. S., Greene, C. A., Blankenship, D. D., Poinar, K., et al. (2018). Basal channels drive active surface hydrology and transverse ice shelf fracture. *Science Advances*, 4(6), eaao7212.

Dupont, T. K., & Alley, R. B. (2005). Assessment of the importance of ice-shelf buttressing to ice-sheet flow. *Geophysical Research Letters*, 32(4). <https://doi.org/10.1029/2004GL022024>

Elvidge, A. D., Renfrew, I. A., King, J. C., Orr, A., Lachlan-Cope, T. A., Weeks, M., & Gray, S. L. (2015). Foehn jets over the Larsen C Ice Shelf, Antarctica. *Quarterly Journal of the Royal Meteorological Society*, 141(688), 698–713.

- Elvidge, A. D., Kuipers Munneke, P., King, J. C., Renfrew, I. A., & Gilbert, E. (2020). Atmospheric drivers of melt on Larsen C ice shelf: Surface energy budget regimes and the impact of foehn. *Journal of Geophysical Research*, *125*(17). <https://doi.org/10.1029/2020jd032463>
- Favier, L., & Pattyn, F. (2015). Antarctic ice rise formation, evolution, and stability. *Geophysical Research Letters*, *42*(11), 2015GL064195.
- Ferrigno, J. G., & Gould, W. G. (1987). Substantial changes in the coastline of Antarctica revealed by satellite imagery. *Polar Record*, *23*(146), 577–583. <https://doi.org/10.1017/s003224740000807x>
- Fürst, J. J., Durand, G., Gillet-Chaulet, F., Tavard, L., Rankl, M., Braun, M., & Gagliardini, O. (2016). The safety band of Antarctic ice shelves. *Nature Climate Change*, *6*(5), 479–482.
- Gagliardini, O., Durand, G., Zwinger, T., Hindmarsh, R. C. A., & Le Meur, E. (2010). Coupling of ice-shelf melting and buttressing is a key process in ice-sheets dynamics. *Geophysical Research Letters*, *37*(14). <https://doi.org/10.1029/2010GL043334>
- Glasser, N. F., Kulessa, B., Luckman, A., Jansen, D., King, E. C., Sammonds, P. R., et al. (2009). Surface structure and stability of the Larsen C ice shelf, Antarctic Peninsula. *Journal of Glaciology*, *55*(191), 400–410.
- Gudmundsson, G. H. (2013). Ice-shelf buttressing and the stability of marine ice sheets. *The Cryosphere*, *7*(2), 647–655.
- Heid, T., & Kääb, A. (2012). Evaluation of existing image matching methods for deriving glacier surface displacements globally from optical satellite imagery. *Remote Sensing of Environment*, *118*, 339–355. <https://doi.org/10.1016/j.rse.2011.11.024>
- Hogg, A. E., & Hilmar Gudmundsson, G. (2017). Impacts of the Larsen-C Ice Shelf calving event. *Nature Climate Change*, *7*(8), 540–542. <https://doi.org/10.1038/nclimate3359>
- Holland, P. R., Corr, H. F. J., Vaughan, D. G., Jenkins, A., & Skvarca, P. (2009). Marine ice in Larsen Ice Shelf. *Geophysical Research Letters*, *36*(11), L11604.
- Holland, P. R., Brisbourne, A., Corr, H. F. J., McGrath, D., Purdon, K., Paden, J., et al. (2015). Oceanic and atmospheric forcing of Larsen C Ice-Shelf thinning. *The Cryosphere*, *9*(3), 1005–1024.
- Howat, I. M., Porter, C., Smith, B. E., Noh, M.-J., & Morin, P. (2019). The Reference Elevation Model of Antarctica. *The Cryosphere*, *13*(2), 665–674. <https://doi.org/10.5194/tc-13-665-2019>
- Hulbe, C. L., LeDoux, C., & Cruikshank, K. (2010). Propagation of long fractures in the Ronne Ice Shelf, Antarctica, investigated using a numerical model of fracture propagation. *Journal of Glaciology*, *56*(197), 459–472.

- Jansen, D., Kulessa, B., Sammonds, P. R., Luckman, A., King, E. C., & Glasser, N. F. (2010). Present stability of the Larsen C ice shelf, Antarctic Peninsula. *Journal of Glaciology*, *56*(198), 593–600.
- Jansen, D., Luckman, A., Kulessa, B., Holland, P. R., & King, E. C. (2013). Marine ice formation in a suture zone on the Larsen C Ice Shelf and its influence on ice shelf dynamics. *Journal of Geophysical Research: Earth Surface*, *118*(3), 1628–1640.
- Jansen, D., Luckman, A. J., Cook, A., Bevan, S., Kulessa, B., Hubbard, B., & Holland, P. R. (2015). Brief Communication: Newly developing rift in Larsen C Ice Shelf presents significant risk to stability. *The Cryosphere*, *9*(3), 1223–1227.
- Jezeq, K. C. (2003). Observing the Antarctic Ice Sheet Using the RADARSAT-1 Synthetic Aperture Radar. *Polar Geography*, *27*(3), 197–209.
- Jezeq, K. C., Sohn, H. G., & Noltimier, K. F. (1998). The RADARSAT Antarctic Mapping Project. *IGARSS '98. Sensing and Managing the Environment. 1998 IEEE International Geoscience and Remote Sensing. Symposium Proceedings. (Cat. No.98CH36174)*. <https://doi.org/10.1109/igarss.1998.702246>
- Joughin, I., Howat, I. M., Fahnestock, M., Smith, B., Krabill, W., Alley, R. B., et al. (2008). Continued evolution of Jakobshavn Isbrae following its rapid speedup. *Journal of Geophysical Research*, *113*(F4). <https://doi.org/10.1029/2008jf001023>
- King, J. C., Kirchgassner, A., Bevan, S., Elvidge, A. D., Kuipers Munneke, P., Luckman, A., et al. (2017). The Impact of Föhn Winds on Surface Energy Balance During the 2010–2011 Melt Season Over Larsen C Ice Shelf, Antarctica. *Journal of Geophysical Research, D: Atmospheres*, *122*(22), 2017JD026809.
- Krug, J., Weiss, J., Gagliardini, O., & Durand, G. (2014). Combining damage and fracture mechanics to model calving. *The Cryosphere*, *8*(6), 2101–2117. <https://doi.org/10.5194/tcd-8-1111-2014>
- Kulessa, B., Jansen, D., Luckman, A. J., King, E. C., & Sammonds, P. R. (2014). Marine ice regulates the future stability of a large Antarctic ice shelf. *Nature Communications*, *5*, 3707.
- Kulessa, B., Booth, A. D., O’Leary, M., McGrath, D., King, E. C., Luckman, A. J., et al. (2019). Seawater softening of suture zones inhibits fracture propagation in Antarctic ice shelves. *Nature Communications*, *10*(1), 5491.
- Lai, C.-Y., Kingslake, J., Wearing, M. G., Chen, P.-H. C., Gentine, P., Li, H., et al. (2020). Vulnerability of Antarctica’s ice shelves to meltwater-driven fracture. *Nature*, *584*(7822), 574–578. <https://doi.org/10.1038/s41586-020-2627-8>
- Larour, E., Seroussi, H., Morlighem, M., & Rignot, E. (2012). Continental scale, high order, high spatial resolution, ice sheet modeling using the Ice Sheet System Model (ISSM). *Journal of Geophysical Research: Earth Surface*, *117*(F1). <https://doi.org/10.1029/2011jf002140>

- Lhermitte, S., Sun, S., Shuman, C., Wouters, B., Pattyn, F., Wuite, J., et al. (2020). Damage accelerates ice shelf instability and mass loss in Amundsen Sea Embayment. *Proceedings of the National Academy of Sciences of the United States of America*, *117*(40), 24735–24741.
- Lipovsky, B. P. (2020). Ice shelf rift propagation: stability, three-dimensional effects, and the role of marginal weakening. *The Cryosphere*, *14*(5), 1673–1683. <https://doi.org/10.5194/tc-14-1673-2020>
- Liu, H., Jezek, K., Li, B., & Zhao, Z. (2001). Radarsat Antarctic Mapping Project digital elevation model version 2. *Radarsat Antarctic Mapping Project Digital Elevation Model Version 2, Boulder, Colorado USA: National Snow and Ice Data Center. Digital Media.*
- Liu, H., Wang, L., Tang, S.-J., & Jezek, K. C. (2012). Robust multi-scale image matching for deriving ice surface velocity field from sequential satellite images. *International Journal of Remote Sensing*, *33*(6), 1799–1822.
- Liu, Y., Moore, J. C., Cheng, X., Gladstone, R. M., Bassis, J. N., Liu, H., et al. (2015). Ocean-driven thinning enhances iceberg calving and retreat of Antarctic ice shelves. *Proceedings of the National Academy of Sciences of the United States of America*, *112*(11), 3263–3268.
- Luckman, A., Elvidge, A., Jansen, D., Kulesa, B., Munneke, P. K., King, J., & Barrand, N. E. (2014). Surface melt and ponding on Larsen C Ice Shelf and the impact of föhn winds. *Antarctic Science / Blackwell Scientific Publications*, *26*(6), 625–635.
- MacAyeal, D. R. (1989). Large-scale ice flow over a viscous basal sediment: Theory and application to ice stream B, Antarctica. *Journal of Geophysical Research*, *94*(B4), 4071–4087.
- MacAyeal, D. R., Scambos, T. A., Hulbe, C. L., & Fahnestock, M. A. (2003). Catastrophic ice-shelf break-up by an ice-shelf-fragment-capsize mechanism. *Journal of Glaciology*, *49*(164), 22–36.
- Matsuoka, K., Hindmarsh, R. C. A., Moholdt, G., Bentley, M. J., Pritchard, H. D., Brown, J., et al. (2015). Antarctic ice rises and rumples: Their properties and significance for ice-sheet dynamics and evolution. *Earth-Science Reviews*, *150*, 724–745.
- McGrath, D., Steffen, K., Holland, P. R., Scambos, T., Rajaram, H., Abdalati, W., & Rignot, E. (2014). The structure and effect of suture zones in the Larsen C Ice Shelf, Antarctica. *Journal of Geophysical Research: Earth Surface*, *119*(3), 588–602.
- Morland, L. W. (1987). Unconfined Ice-Shelf Flow. In *Dynamics of the West Antarctic Ice Sheet* (pp. 99–116). Springer Netherlands.
- Morlighem, M., Seroussi, H., Larour, É., Schlegel, N., Borstad, C., de Fleurian, B., et al. (2015). Ice sheet system model 2015 (4.9) user guide. Retrieved June

30, 2021, from <http://www.ccpo.odu.edu/~klinck/Reprints/PDF/ISSMguide2015.pdf>

Morris, E. M., & Vaughan, D. G. (2003). Spatial and Temporal Variation of Surface Temperature on the Antarctic Peninsula And The Limit of Viability of Ice Shelves. In *Antarctic Peninsula Climate Variability: Historical and Paleoenvironmental Perspectives* (pp. 61–68). American Geophysical Union.

Mouginot, J., Rignot, E., & Scheuchl, B. (2019a). Continent-wide, interferometric SAR phase, mapping of antarctic ice velocity. *Geophysical Research Letters*, *46*(16), 9710–9718.

Mouginot, J., Rignot, E., & Scheuchl, B. (2019b). *MEASUREs Phase-Based Antarctica Ice Velocity Map, Version 1*. [Antarctic Peninsula]. Boulder, Colorado USA. NASA National Snow and Ice Data Center Distributed Active Archive Center. doi: <https://doi.org/10.5067/PZ3NJ5RXHR10>. [Access date: 2020-10-01].

Noble, T. L., Rohling, E. J., Aitken, A. R. A., Bostock, H. C., Chase, Z., Gomez, N., et al. (2020). The sensitivity of the antarctic ice sheet to a changing climate: Past, present, and future. *Reviews of Geophysics*, *58*(4). <https://doi.org/10.1029/2019rg000663>

Paolo, F. S., Fricker, H. A., & Padman, L. (2015). Ice sheets. Volume loss from Antarctic ice shelves is accelerating. *Science*, *348*(6232), 327–331.

Pattyn, F., & Morlighem, M. (2020). The uncertain future of the Antarctic Ice Sheet. *Science*, *367*(6484), 1331–1335.

Pritchard, H. D., Ligtenberg, S. R. M., Fricker, H. A., Vaughan, D. G., van den Broeke, M. R., & Padman, L. (2012). Antarctic ice-sheet loss driven by basal melting of ice shelves. *Nature*, *484*(7395), 502–505.

Reese, R., Gudmundsson, G. H., Levermann, A., & Winkelmann, R. (2017). The far reach of ice-shelf thinning in Antarctica. *Nature Climate Change*, *8*(1), 53–57.

Rignot, E., Casassa, G., Gogineni, P., Krabill, W., Rivera, A., & Thomas, R. (2004). Accelerated ice discharge from the Antarctic Peninsula following the collapse of Larsen B ice shelf. *Geophysical Research Letters*, *31*(18), L18401.

Rignot, E., Jacobs, S., Mouginot, J., & Scheuchl, B. (2013). Ice-shelf melting around Antarctica. *Science*, *341*(6143), 266–270.

Robel, A. A., & Banwell, A. F. (2019). A speed limit on ice shelf collapse through hydrofracture. *Geophysical Research Letters*, *46*(21), 12092–12100.

Rott, H., Skvarca, P., & Nagler, T. (1996). Rapid collapse of northern Larsen ice shelf, Antarctica. *Science*, *271*(5250), 788.

Scambos, T., Hulbe, C., & Fahnestock, M. (2003). Climate-induced ice shelf disintegration in the Antarctic peninsula. *Antarctic Peninsula Climate Variability:*

*Historical and Paleoenvironmental Perspectives*, 79–92.

Scambos, T., Fricker, H. A., Liu, C.-C., Bohlander, J., Fastook, J., Sargent, A., et al. (2009). Ice shelf disintegration by plate bending and hydro-fracture: Satellite observations and model results of the 2008 Wilkins ice shelf break-ups. *Earth and Planetary Science Letters*, *280*(1), 51–60.

Scambos, T. A., Dutkiewicz, M. J., Wilson, J. C., & Bindshadler, R. A. (1992). Application of image cross-correlation to the measurement of glacier velocity using satellite image data. *Remote Sensing of Environment*, *42*(3), 177–186.

Scambos, T. A., Hulbe, C., Fahnestock, M., & Bohlander, J. (2000). The link between climate warming and break-up of ice shelves in the Antarctic Peninsula. *Journal of Glaciology*, *46*(154), 516–530.

Scambos, T. A., Bohlander, J. A., Shuman, C. A., & Skvarca, P. (2004). Glacier acceleration and thinning after ice shelf collapse in the Larsen B embayment, Antarctica. *Geophysical Research Letters*, *31*(18), L18402.

Shepherd, A., Wingham, D., Payne, T., & Skvarca, P. (2003). Larsen ice shelf has progressively thinned. *Science*, *302*(5646), 856–859.

Skvarca, P. (1994). Changes and surface features of the Larsen Ice Shelf, Antarctica, derived from Landsat and Kosmos mosaics. *Annals of Glaciology*, *20*, 6-12. <https://doi.org/10.3189/1994aog20-1-6-12>

Small, D., Schubert, A., Rosich, B., Meier, E., Lacoste, H., & Ouwehand, L. (2007). Geometric and radiometric correction of ESA SAR products. In H. Lacoste & L. Ouwehand (Eds.) (p. online). Presented at the Envisat Symposium 2007, Montreux (CH): European Space Agency \* Communication Production Office.

Thomas, R. H. (1979). Ice Shelves: A Review. *Journal of Glaciology*, *24*(90), 273–286.

Vaughan, D. G., & Doake, C. S. M. (1996). Recent atmospheric warming and retreat of ice shelves on the Antarctic Peninsula. *Nature*, *379*(6563), 328–331.

Vaughan, D. G., Marshall, G. J., Connolley, W. M., Parkinson, C., Mulvaney, R., Hodgson, D. A., et al. (2003). Recent Rapid Regional Climate Warming on the Antarctic Peninsula. *Climatic Change*, *60*(3), 243–274.

Vieli, A., Payne, A. J., Shepherd, A., & Du, Z. (2007). Causes of pre-collapse changes of the Larsen B ice shelf: Numerical modelling and assimilation of satellite observations. *Earth and Planetary Science Letters*, *259*(3), 297–306.

Wang, S., Liu, H., Yu, B., Zhou, G., & Cheng, X. (2016). Revealing the early ice flow patterns with historical Declassified Intelligence Satellite Photographs back to 1960s. *Geophysical Research Letters*, *43*(11), 2016GL068990.

Wang, S., Alexander, P., Wu, Q., Tedesco, M., & Shu, S. (2021). Characterization of ice shelf fracture features using ICESat-2 – A case study over the Amery

Ice Shelf. *Remote Sensing of the Environment*, 255, 112266.

Weis, M., Greve, R., & Hutter, K. (1999). Theory of shallow ice shelves. *Continuum Mechanics and Thermodynamics*, 11(1), 15–50.

**Controls on Larsen C Ice Shelf retreat from a 60-year satellite data record**

Shujie Wang<sup>1,2,3</sup>, Hongxing Liu<sup>4,5</sup>, Kenneth Jezek<sup>6</sup>, Richard B. Alley<sup>2,7</sup>, Lei Wang<sup>8</sup>, Patrick Alexander<sup>9</sup>, and Yan Huang<sup>5</sup>

<sup>1</sup>Department of Geography, Pennsylvania State University, University Park, PA 16802, USA.

<sup>2</sup>Earth and Environmental Systems Institute, Pennsylvania State University, University Park, PA 16802, USA.

<sup>3</sup>Institute for Computational and Data Sciences, Pennsylvania State University, University Park, PA 16802, USA.

<sup>4</sup>Department of Geography, University of Alabama, Tuscaloosa, AL 35487, USA.

<sup>5</sup>Key Laboratory of Geographic Information Science, Ministry of Education, East China Normal University, Shanghai 200241, China.

<sup>6</sup>School of Earth Sciences, Ohio State University, Columbus, OH 43210, USA.

<sup>7</sup>Department of Geosciences, Pennsylvania State University, University Park, PA 16802, USA.

<sup>8</sup>Department of Geography & Anthropology, Louisiana State University, Baton Rouge, LA 70803, USA.

<sup>9</sup>Lamont-Doherty Earth Observatory, Columbia University, Palisades, NY 10964, USA.

**Contents of this file**

Text S1 to S2

Figures S1

Tables S1

## **Introduction**

This supporting document includes more details about the preprocessing of satellite imagery (Text S1) and ice shelf modeling (Text S2), one supplementary figure (Figure S1), and one table (Table S1). Figure S1 shows the time series of Larsen C front locations from 1963 to 2020. Table S1 provides detailed information on the image sources, time periods, and estimated accuracies for flow velocity derivation over multiple periods.

### **Text S1. Satellite images and preprocessing**

The images we used for this study include declassified intelligence satellite photographs (DISP) acquired by the ARGON mission, optical images acquired by the Landsat-4/5 TM, Landsat-7 ETM+, and Landsat-8 OLI sensors, and synthetic aperture radar (SAR) images acquired by the ERS-1, ERS-2, Radarsat-1, Envisat, and ALOS satellites.

The DISP images were acquired by the ARGON KH-5 panchromatic camera from an orbital altitude of 322 km at a ground resolution of 140 m. Trackable features such as crevasses, rifts, and flow bands are visible on the images. We orthorectified the DISP images using a rigorous camera model with bundle block adjustment based on a set of ground control points (GCPs) selected from very high-resolution WorldView images (Wang et al., 2016). The Landsat images were provided as L1G or L1GT products via the USGS EarthExplorer data portal, and were georeferenced and orthorectified by the USGS EROS data center. The Radarsat-1 images were orthorectified and mosaiced by the Byrd Polar and Climate Research Center for the Radarsat Antarctic Mapping Project (RAMP) (Jezek et al., 1998; Jezek, 2003). The ALOS PALSAR images were accessed from the Alaska Satellite Facility data portal, and were geocoded and orthorectified by the Japan Aerospace Exploration Agency. The ERS-1, ERS-2, and Envisat SAR images were provided by the European Space Agency. We geocoded and orthorectified these SAR images using the PRARE precise orbit data for ERS-1/2 and the DORIS precise orbit data for Envisat in the ENVI® SARscape® software. The RAMP digital elevation model 2 (Liu et al., 2001) was used for image orthorectification. The accuracy of geolocation using the precise orbit data is estimated to be better than one pixel (Small et al., 2007). The speckle noise of SAR imagery was suppressed by applying gamma and median filters. For images used for velocity derivation, we also conducted image-to-image co-registration for each image pair to ensure the relative error of image alignment is less than one pixel. To enhance the surface features on imagery for velocity mapping, we divided each image pair into multiple segment pairs and performed image histogram stretching.

## Text S2. Ice shelf modeling experiments

We used the Ice-sheet and Sea-level System Model (ISSM), developed by the Jet Propulsion Laboratory and the University of California at Irvine (Larour et al., 2012), to conduct the ice shelf modeling experiments. We used the shallow shelf approximation (SSA) model (MacAyeal 1989; Weis et al. 1999; Morland 1987) to examine how ice shelf flow velocities and stress conditions vary with front retreat and rift development. The SSA model assumes a hydrostatic equilibrium condition and depth-invariant horizontal velocity, described as:

$$\frac{\partial}{\partial x} \left( 2\eta h \left( 2 \frac{\partial u}{\partial x} + \frac{\partial v}{\partial y} \right) \right) + \frac{\partial}{\partial y} \left( \eta h \left( \frac{\partial u}{\partial y} + \frac{\partial v}{\partial x} \right) \right) = \rho g h \frac{\partial s}{\partial x} \quad (1)$$

$$\frac{\partial}{\partial y} \left( 2\eta h \left( 2 \frac{\partial v}{\partial y} + \frac{\partial u}{\partial x} \right) \right) + \frac{\partial}{\partial x} \left( \eta h \left( \frac{\partial u}{\partial y} + \frac{\partial v}{\partial x} \right) \right) = \rho g h \frac{\partial s}{\partial y} \quad (2)$$

where  $x$  and  $y$  are horizontal cartesian coordinates,  $u$  and  $v$  are the velocity components in the  $x$  and  $y$  directions,  $g$  is the gravitational acceleration ( $9.81 \text{ m/s}^2$ ),  $h$  is the ice thickness,  $s$  is the surface elevation,  $\rho$  is the ice density ( $916 \text{ kg/m}^3$ ), and  $\eta$  is the effective viscosity given by:

$$\eta = \frac{1}{2} \bar{B} \left[ \left( \frac{\partial u}{\partial x} \right)^2 + \left( \frac{\partial v}{\partial y} \right)^2 + \frac{\partial u}{\partial x} \frac{\partial v}{\partial y} + \frac{1}{4} \left( \frac{\partial u}{\partial y} + \frac{\partial v}{\partial x} \right)^2 \right]^{(1-n)/2n} \quad (3)$$

where  $\bar{B}$  is the vertically averaged hardness and represents the ice rigidity, and  $n$  is Glen's flow law exponent.

ISSM is based on a finite element numerical modeling scheme. The ice rigidity parameter  $\bar{B}$  can be solved for through inversion by minimizing the differences between modeled and observed flow velocities. For model configuration, we used the anisotropic mesh adaptation method to generate the numerical mesh net nodes. The surface elevations were obtained from the Antarctic digital elevation model created from ERS-1 radar and ICESat laser altimetry data (Bamber et al., 2009). The ice shelf thickness ( $h$ ) was calculated based on the hydrostatic equilibrium condition:

$$h = \left( \frac{\rho'}{\rho' - \rho} \right) \times s \quad (4)$$

where  $\rho'$  is the seawater density ( $1028 \text{ kg/m}^3$ ),  $s$  is the surface elevation, and  $\rho$  is the ice density ( $916 \text{ kg/m}^3$ ).

Using the modeled flow velocity field and parameter  $\bar{B}$ , we calculated the deviatoric stresses, including longitudinal deviatoric stresses, first principal stresses, and second principal stresses. The deviatoric stress ( $\tau$ ) is calculated as:

$$\tau = 2\eta \dot{\epsilon} \quad (5)$$

where  $\eta$  is the effective viscosity (equation 3), and  $\dot{\epsilon}$  is the corresponding strain rate. In a horizontal Cartesian system, the strain rates ( $\dot{\epsilon}_x, \dot{\epsilon}_y, \dot{\epsilon}_{xy}$ ) are calculated as:

$$\dot{\epsilon}_x = \frac{\partial u}{\partial x} \quad (6)$$

$$\dot{\epsilon}_y = \frac{\partial v}{\partial y} \quad (7)$$

$$\dot{\epsilon}_{xy} = \frac{1}{2} \left( \frac{\partial u}{\partial y} + \frac{\partial v}{\partial x} \right) \quad (8)$$

Following Alley et al. (2018), the longitudinal strain rate ( $\dot{\epsilon}_{lon}$ , along the flow direction) can be calculated as:

$$\dot{\epsilon}_{lon} = \dot{\epsilon}_x \cos^2 \alpha + 2\dot{\epsilon}_{xy} \cos \alpha \sin \alpha + \dot{\epsilon}_y \sin^2 \alpha \quad (9)$$

where  $\alpha$  is the flow angle that is counter-clockwise from the x axis.

The magnitudes of the maximum ( $\dot{\epsilon}_{first}$ , first principal) and minimum ( $\dot{\epsilon}_{second}$ , second principal) tensile principal strain rates can be calculated as:

$$\dot{\epsilon}_{first} = \frac{1}{2}(\dot{\epsilon}_x + \dot{\epsilon}_y) + \sqrt{\frac{1}{4}(\dot{\epsilon}_x - \dot{\epsilon}_y)^2 + \dot{\epsilon}_{xy}^2} \quad (10)$$

$$\dot{\epsilon}_{second} = \frac{1}{2}(\dot{\epsilon}_x + \dot{\epsilon}_y) - \sqrt{\frac{1}{4}(\dot{\epsilon}_x - \dot{\epsilon}_y)^2 + \dot{\epsilon}_{xy}^2} \quad (11)$$

$$\theta = \frac{1}{2} \left[ \arctan \left( \frac{2\dot{\epsilon}_{xy}}{\dot{\epsilon}_x - \dot{\epsilon}_y} \right) \right] \quad (12)$$

where  $\theta$  is the angle between the y axis and the first principal axis if  $\dot{\epsilon}_x < \dot{\epsilon}_y$ , or between the y axis and the second principal axis if  $\dot{\epsilon}_x > \dot{\epsilon}_y$ .

Following Cuffey and Paterson (2010), the backstress ( $\sigma_b$ ) can be calculated as

$$\sigma_b = \frac{1}{2} \rho g \left( 1 - \frac{\rho}{\rho'} \right) h - 2\eta(2\dot{\epsilon}_x + \dot{\epsilon}_y) \quad (13)$$

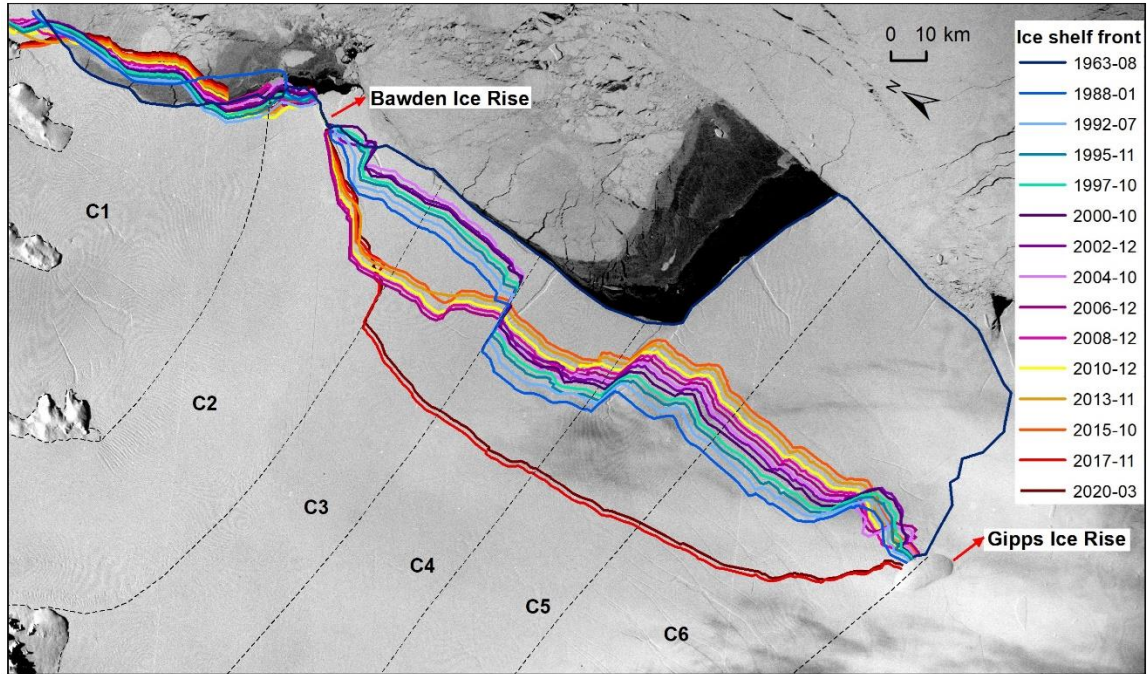


**Figure S1.** Ice front locations of Larsen C from 1963 to 2020. The background image is the georeferenced DISP image acquired in 1963.

Period	Image source	Displacement uncertainty (m)	Time separation (years)	Velocity uncertainty (m/year)
1963/08–1988/01	DISP, Landsat TM	90	24.4	3.7
1986/03–1988/01	Landsat TM	45	1.8	25
1997/10–2000/09	Radarsat SAR	37.5	3.0	12.5
2000/01–2002/12	Landsat ETM+	22.5	1.9	11.8
2006/06–2008/10	ALOS PALSAR	22.5	2.4	9.4
2008/10–2010/10	ALOS PALSAR	22.5	2.0	11.3
2013/11–2015/11	Landsat OLI	22.5	2.0	11.3
2015/11–2016/12	Landsat OLI	22.5	1.1	20.5
2016/12–2017/12	Landsat OLI	22.5	1.0	22.5
2017/12–2019/02	Landsat OLI	22.5	1.3	17.3
2019/02–2020/03	Landsat OLI	22.5	1.1	20.5

**Table S1.** Image sources, time periods, and estimated uncertainties for ice velocity derivation.